Structural interhemispheric connectivity defects in mouse models of BBSOAS: Insights from high spatial resolution 3D white matter tractography

Jean Christophe Deloulme [a,1], Maxime Leclercq [b,1], Olivier Deschaux [c], Gemma Flore [d], Laetitia Capellano [a], Chiara Tocco [c], Barbara Yael Braz [a], Michèle Studer [c,*,2], Hana Lahrech [b,2]

[a] *Univ. Grenoble Alpes, Inserm, U1216, Grenoble Institute Neurosciences, 38000 Grenoble, France*
[b] *BrainTech Lab Inserm U1205, Grenoble, France*
[c] *University Côte d'Azur (UCA), CNRS, Inserm, Institute of Biology Valrose (iBV), Nice, France*
[d] *Institute of Genetics and Biophysics "Adriano Buzzati Traverso", CNR, Napoli, Italy*

ABSTRACT

White matter (WM) tract formation and axonal pathfinding are major processes in brain development allowing to establish precise connections between targeted structures. Disruptions in axon pathfinding and connectivity impairments will lead to neural circuitry abnormalities, often associated with various neurodevelopmental disorders (NDDs). Among several neuroimaging methodologies, Diffusion Tensor Imaging (DTI) is a magnetic resonance imaging (MRI) technique that has the advantage of visualizing in 3D the WM tractography of the whole brain non-invasively. DTI is particularly valuable in unpinning structural tract connectivity defects of neural networks in NDDs. In this study, we used 3D DTI to unveil brain-specific tract defects in two mouse models lacking the *Nr2f1* gene, which mutations in patients have been proven to cause an emerging NDD, called Bosch-Boonstra-Schaaf Optic Atrophy (BBSOAS). We aimed to investigate the impact of the lack of cortical *Nr2f1* function on WM morphometry and tract microstructure quantifications. We found in both mutant mice partial loss of fibers and severe misrouting of the two major cortical commissural tracts, the corpus callosum, and the anterior commissure, as well as the two major hippocampal efferent tracts, the post-commissural fornix, and the ventral hippocampal commissure. DTI tract malformations were supported by 2D histology, 3D fluorescent imaging, and behavioral analyses. We propose that these interhemispheric connectivity impairments are consistent in explaining some cognitive defects described in BBSOAS patients, particularly altered information processing between the two brain hemispheres. Finally, our results highlight 3DDTI as a relevant neuroimaging modality that can provide appropriate morphometric biomarkers for further diagnosis of BBSOAS patients.

1. Introduction

Bosch-Boonstra-Schaaf Optic Atrophy syndrome (BBSOAS; OMIM 615722; ORPHA 401777) is a rare autosomal dominant neurodevelopmental disorder (NDD) with an estimated prevalence between 1 in 100,000 to 250,000 people worldwide, and caused by haploinsufficiency of the *NR2F1* gene (also known as *COUP-TFI*), a key transcriptional regulator of brain development (Bosch et al., 2014; Chen et al., 2016; Rech et al., 2020; Bertacchi et al., 2022). Patients carrying mutations in the *NR2F1* gene typically show a combination of cognitive

symptoms, such as developmental delays, intellectual disability, speech and language difficulties, motor dysfunctions, autism spectrum disorder (ASD), but also signs of cortical visual impairments, hypotonia, seizures, and others (Rech et al., 2020; Bertacchi et al., 2022; Billiet et al., 2022). Several mouse models of loss-of-function have demonstrated that *Nr2f1* plays key roles in regulating major brain developmental processes, from proliferation and differentiation of neural progenitors to cell migration and axonal projections of cortical neurons (reviewed in (Tocco et al., 2021)). In particular, constitutive *Nr2f1null* pups show axonal elongation and somatotopic defects of the major brain commissures

(Armentano et al., 2006; Alfano et al., 2011), and of the retino-geniculo-cortical visual pathway (Armentano et al., 2007; Chou et al., 2013; Bertacchi et al., 2020; Tocco et al., 2022).

The data obtained by histological and molecular analyses, axonal tracing, and/or cell-type specific reporter mouse lines have highlighted some of the major roles that *Nr2f1* plays in establishing brain circuitry and function during development. However, very little is known about the progression of these early defects and whether axonal impairments are maintained or corrected in adult stages, an important issue if we wish to correlate mouse studies to human BBSOAS pathology. In addition, these data are still incomplete in delivering an exhaustive 3D view of axonal tract projections that could be very useful for the identification of patient brain malformations. Histological analyses in 2D sections suggest consistent abnormalities, but interpretations of many observations can remain limited and localized and thus, require specific 3D imaging validations. Neuroimaging modalities are now unavoidable for precise diagnosis allowing whole brain visualization, its microstructure, and function (O'Connell et al., 2023). Diffusion Tensor Imaging (DTI), which is a magnetic resonance imaging (MRI) technique has acquired a growing interest in studying the whole brain, its structure and organization, and more specifically the white matter (WM) fiber tracking imaging. Here, we use morphometric parameters such as the number of streamlines, thickness, surface area, and volume of neuronal tracts to assess and quantify the impact of genetic ablation of *Nr2f1* in neurons on WM organization and neuronal connectivity in adult mice. Hence, 3D DTI significantly increases our understanding of brain connectivity, called tractography (Calamante, 2017), and more interestingly, it paves a way to identify and study the pathophysiological conditions that could be at the origin of damages and abnormalities in WM tracts of various neurological and psychiatric disorders (Yen et al., 2023).

In this study, we used microscopic DTI to visualize in 3D the overall defects of WM tracts on two distinct *Nr2f1* cortico-specific *knockout* mouse models, the *Emx1-cKO and Nex-cKO*. While in the *Emx1-cKO* line, *Nr2f1* expression is abolished from early cortical progenitor cells at embryonic stage (E) 9.5 (Armentano et al., 2007), in the *Nex-cKO* mouse model, *Nr2f1* expression is inactivated at later stages (E11.5-E12), specifically in cortical postmitotic neurons (Alfano et al., 2014). By comparing these two lines, we aimed to pinpoint the origin of the tract defects and understand whether *Nr2f1* acts in mitotic, post-mitotic, or both cell types. Previous studies in cortical areal organization and thalamocortical connectivity (Alfano et al., 2014), hippocampal morphogenesis (Flore et al., 2017; Parisot et al., 2017), and corticopontine projections (Tocco et al., 2022) showed similarities and differences between these two models. Although highly significant, these reports, which were mainly performed at embryonic and early postnatal stages, are found in separate studies without any standardized overview of all morphological and anatomical defects.

The complex behavioral and morphological phenotypes described in *Nr2f1* mouse models are consistent with the heterogeneous symptoms observed in BBSOAS patients, hence sustaining the value of these disease models to further dissect the origin of the syndrome (Tocco et al., 2021). However, we were aware that the few altered axonal tracts previously detected in these mouse lines, could not reflect the full repertoire of phenotypic impairments described in patients (Bertacchi et al., 2022). Consequently, the major aim of this study was to obtain a fully comprehensive representation of cortico-specific axonal tracts in conditional adult mice lacking *Nr2f1* solely in the cortex by using the DTI approach to obtain a 3D view of axonal tracts. Our experimental protocol using these two mouse models aimed to compare mitotic *versus* postmitotic roles of *Nr2f1* in axonal connectivity and tract formation. Overall, our present study has unveiled new defects in the integrity and connectivity of several major commissural fibers. Moreover, the results of the present study have contributed to discerning the influence of *Nr2f1* in progenitors or neurons during the differentiation, guidance, and maturation of fiber tracts.

2. Materials and methods

2.1. Ethical approval and mice

All animal experiments were conducted in accordance with the French Animal Welfare Act and European guidelines (directive 2010/63/EU) for the use of experimental animals, using protocols approved by the French Ministry of Education, Research and Innovation (APAFIS# 8019–2,018,112,919,027,679 and 8303–2,016,060,110,523,424) and the local ethics committee in Nice (CIEPAL NCE/2019–548) and Grenoble (CIEPAL GIN, C2EA-04). Every precaution was taken to minimize the number of animals used and the stress on animals during experiments. Adult control (over 2 months old) and their littermate mutant mice were used for experiments and housed 2 or 3 per cage with the recommended environmental enrichment (wooden cubes, cotton pad, igloo). Behavioral testing was performed during the light phase of our 12 h light-dark cycle (light on at 7:00 and off at 19:00) animal facility with food and water *ad libitum*, except during the novelty suppressed feeding test. The two cortex-specific conditional mice, referred to as *Emx1-cKO* and *Nex-cKO*, were generated by crossing *Nr2f1lox/lox* mice with *Nr2f1lox/lox/Emx1-Cre* or *Nr2f1lox/lox/Nex-Cre* mice as previously described (Armentano et al., 2006; Armentano et al., 2007; Alfano et al., 2014). Half of the generated mice will be *Nr2f1lox/lox* and designated as control mice, identical for both groups. Adult transgenic males and females (between 2 and 5 months) were used for the histological (24 mice), for neuroimaging (26 mice) and for behavioral (up to 30 mice) experiments in the present study. The different mouse groups were independent but had the same background strain (C57BL/6 J). The number of mice used in each experimental approach is listed in **Table S1**.

2.2. Diffusion Tensor Imaging (DTI)

DTI is an MRI method that exploits the properties of water diffusion in an anisotropic medium. In the brain, DTI is sensitive to the microarchitecture of WM and gray matter (GM). We measure three diffusivity eigenvalues (also called apparent diffusion coefficients, ADC) and their corresponding eigenvectors. In GM, the diffusion is isotropic: the three values are equal, while in WM it is anisotropic, relatively free along the axonal axis, (largest value) and restricted perpendicularly (lowest values). These differences are quantified by the fractional anisotropy parameter (FA) and discriminate WM from GM. In WM, the eigenvector associated with the largest diffusivity is called the primary eigenvector and indicates the fiber axis orientation. Three DTI-derived images are used in this study: FA maps where pixels with high FA correspond to WM; FA color maps which combine FA information and the primary eigenvector direction defined by a color code; the fiber tracking imaging, where pixels with low FA (*i.e.,* GM) are dark and pixels with high FA (*i.e.,* WM) are depicted with lines having the primary eigenvector direction with directionally encoded color (Alexander et al., 2007; Jiang and Johnson, 2010).

2.3. Brain preparation for ex vivo DTI acquisitions

DTI acquisitions were performed on brains *ex vivo*. Skulls containing intact brains were prepared as previously described (Gimenez et al., 2016; Gimenez et al., 2017). Briefly, mice were transcardially perfused with a solution containing 4% paraformaldehyde (PFA) in phosphate-buffered (PBS), and with 6.25 mM of Gd-DOTA, a paramagnetic contrast agent used here to reduce longitudinal relaxation T_1 in order to accelerate MRI acquisitions to obtain 3D acquisitions. After removing surrounding skin and muscles, the skulls containing intact brains were immersed in the fixing solution for four days, and then transferred to a Fomblin (FenS chemicals) bath for 11 days after brain fixation. This experimental protocol provided homogeneous distribution of the Gd-DOTA throughout the whole brain. We used Fomblin, which is a

perfluoropolyether oil to avoid any MRI susceptibility artefacts at the interface of air and water.

2.4. 3D DTI acquisitions

Microscopic 3D MRI acquisitions were performed *ex vivo* at 9.4 T (Avance III console, Bruker – Grenoble IRMaGe facility) using a volume coil for transmission and a head surface cryocoil for reception. 3D spin-echo DTI sequence with Cartesian K-space sampling was used. Isotropic high spatial resolution of 80 μm was obtained in a field of view of 15.2 × 1.2. 24 × 10.08 mm^3. The repetition time, echo time and number of accumulations were set to 90 ms, 18.37 ms and 4, respectively. Diffusion gradients were applied with duration δ = 4 ms and a separation duration Δ = 8,1 ms, in 6 different spatial orientations [1,1,0]; [0,1,1]; [1,0,1]; [1,−1,0]; [0,1,−1]; [−1,0,1] with a gradient factor (b-value) of 1700 s/mm^2. The reference diffusion image (b$_0$-reference image or anatomical T$_{2W}$ image) was acquired with a low b-value equal to 30 s/mm^2 in order to suppress possible artefacts that can appear in the presence of imperfections of refocused 180° pulse of spin echo sequence. The total duration of the microscopic 3D DTI scan was 10 h 14 min with a signal-to-noise ratio (SNR) around 100. MRI acquisition and reconstruction were performed using Paravision v7.0.0 (Bruker, Ettlingen, Germany). Spin echo was used rather than echo planar imaging (EPI) sequence to avoid geometric distortions, and low angular resolution with signal accumulations was preferred to favor SNR, which is crucial in the case of mice having a very small brain volume. Our method realized *ex vivo* has already demonstrated its usefulness in reconstructing major WM tracts and detecting their changes by volume quantification (Deloulme et al., 2015; Gimenez et al., 2017).

2.5. Brain volume measurement

Total brain volumes were defined by MRI segmentation on the b$_0$-reference images. Brains were manually segmented using Fiji software, specifically employing the Segmentation Editor plug-in (http://fiji.sc/Segmentation_Editor), as described by Gimenez et al. (2017). A total number of 26 mice was used, corresponding to *n* = 10 for control (*Ctrl*), n = 10 for *Emx1-cKO*, and *n* = 6 for *Nex-cKO* mice.

2.6. DTI processing and fiber tracking

3D DTI fiber tracking of the WM of the whole brain was first constructed for each mouse providing thereafter, the reconstruction of each specific tract. Quantitative parameters, such as WM tract volumes, the number of WM fibers, here denoted streamline fiber tracts, and number of branches and fasciculations were quantified to evaluate WM tract changes between mouse groups. 3D fiber tractography was obtained by using the DTI track module of MedINRIA software (version 1.9.4; http://med.inria.fr/) (Fillard and Toussaint, 2006). First, the three diffusivity eigenvalues and their corresponding eigenvectors, as well as the fractional anisotropy (FA) indexes, were generated pixelwise. The 3D tractography of WM fibers was computed using the Tensor Toolkit software. First GM structures characterized by low FA values were suppressed by applying two threshold FA values which were fixed after several preliminary analyses to discriminate between WM and GM: FA$_1$ = 0.4 used as the initial point to start the fiber reconstruction and FA$_2$ = 0.28 used as the cutoff value to stop fiber propagation. A whole-brain tractogram was then obtained using one seed point per voxel (*i.e.*, 1/(0.080 × 0.080 × 0.080) = 1950 seeds per mm^3). Each specific WM fiber tract structure was derived from the whole-brain tractogram by using two ROIs drawn manually on the b$_0$-reference images. One was used to select the fibers, while the other was used to exclude fibers potentially contaminating the selected tract). The thickness of the genu of the corpus callosum is measured using the Fiji application on b$_0$-reference image from the coronal plane corresponding to a Bregma position of 1.10 mm. ROI positions were defined according to the coordinates

extracted from the Paxinos mouse Atlas (Franklin and Paxinos, 2008). Twelve tracts were mapped using this reconstruction strategy (**Table S2**). Since the total brain volume of *Emx-cKO* and *Nex-cKO* mice did not significantly differ from control mice (463 ± 20 mm^3, 438 ± 25 mm3 and 455 ± 32 mm3; *p* = 0,7609 and p = 0,4111 respectively; Kruskal-Wallis test) and some tracts, such as the retroflex fasciculus, were not altered by genetic recombination, we express the volume and number of streamlines of neuronal tracts in raw, non-normalized values. A total number of 26 mice was used, corresponding to *n* = 10 for control (*Ctrl*), n = 10 for *Emx1-cKO* and *n* = 6 for *Nex-cKO* mice.

2.7. 2D Histology

All stereotaxic coordinates and abbreviations used in this study are derived from Paxinos' adult mouse atlas (Franklin and Paxinos, 2008). The identification and definition of adult brain subregions were based on the atlas, literature, and on cytoarchitectonic characteristics of the different areas (*i.e.*, cell shape or orientation). We have delineated the areas in the main figures. A total number of 12 mice was used, corresponding to n = 6 for control (*Ctrl*) and n = 6 for *Emx1-cKO*.

2.7.1. Nissl staining with Cresyl Violet

The adult mice were overdosed with sodium pentobarbital (100 mg/kg, *i.p.*) and perfused transcardially with 0.1 M PBS (Sinopharm) followed by PBS containing 4% PFA (Sigma). The brains were carefully extracted from the skull and post-fixed overnight with freshly prepared PFA 4% in PBS. Fixed brains that were not used immediately, were stored at 4 °C in 0.0025% NaNO$_3$. Brains were embedded in 4% low-melting agarose (Life Technologies). Mouse brains were vibratome-sectioned coronally with a thickness of 50 μm. Serial sections spanning 200 μm each other were collected on slices and processed for Nissl staining. Briefly, slices were post-fixed in 4% PFA for 10 min and incubated in the staining solution (0.025% thionin, 0.025% Cresyl Violet, 100 mM sodium acetate, 8 mM acetic acid, in deionized H$_2$O) for 5 min at room temperature. Visualization was carried out in the decoloration solution (80% ethanol, 20% deionized H$_2$O and a few drops of acetic acid).

2.7.2. Optical imaging

Pictures were taken using a bright-field microscope (Leica DMI6000B, acquisition software LAS AF 2.6 or LEICA MZ 16 FA Stereomicroscope) equipped with a color camera for *in situ* hybridization and Nissl staining. Small-volume computational clearing was used to remove the background signal derived from out-of-focus blur. Images were digitally documented with the camera provided by the microscope and computer-processed using Adobe Photoshop version 6 for Windows.

2.7.3. Morphometric histological analysis

The morphometric analysis has been done on the whole extent of the reported regions. Nissl-stained tissue sections were identified with serial numbers and matched at the same Bregma level. 14 sections have been considered for the anterior commissure (from Bregma 2.10 to Bregma −0.46 mm), while 25 sections have been considered for the piriform cortex (from Bregma 2.46 *to* Bregma − 2.80 mm*). For the anterior part of anterior commissure (aca from Bregma 2.10 to −0.10 mm) and the posterior part of anterior commissure (acp from Bregma 0.26 to −0.46 mm), surface and number of branches were measured in both hemispheres of control (*n* = 6) and *Emx1-cKO* (n = 6) mice. For the piriform cortex, the entire surface and length as well as specific surface and fragmentation of layer II were measured on one hemisphere of control (n = 6) and *Emx1-cKO* mice. The piriform cortex (Pir) can be subdivided into two regions: anterior (APir) and posterior (PPir) parts along the anterior-posterior axis. The borderline between APir and PPir is defined by the disappearance of the lateral olfactory tract (lo) and the thickened layer III in the PPir (Bregma 0.02 mm) (Loscher and Ebert, 1996; Yang and Sun, 2015). Morphologically, the Pir is easily distinguishable in

coronal sections due to its peculiar tri-laminar organization; while layer I is composed of sparse cells, layer II is clearly detectable thanks to the high density of cell bodies. The different components measured were labeled with a color-coded graphic pen using Image J software (NIH) (Schneider et al., 2012) (Plugins: Analyze-Measure and Label) at 10× and 20× magnifications, based on standard atlases (Franklin and Paxinos, 2008) and cytoarchitectonic features (Neville and Haberly, 2004).

2.7.4. 3D histology of cleared brains

Whole brains from *Ctrl/Thy1-eYFP-H* (*n* = 7) and *Nex-cKO/Thy1-eYFP-H* (*n* = 5) mice were cleared using a protocol published by Boulan et al. (Boulan et al., 2021). Cleared brains were 3D-imaged on a light-sheet fluorescence microscope (Ultramicroscope II, LaVision BioTec, Bielefeld, Germany) using a 2 x long working distance air objective lens (WD 6 mm with the dipping cap) and ImspectorPro software (LaVision BioTec). Acquisitions were performed with a constant lightsheet thickness of 3.93 µm (x = 4.8; y = 4.8; z = 3 µm). 3D volume images were generated using Imaris software (version 9.6, Bitplane) (Oxford Instrument, Gometz-la-Ville, France). Fornices were manually segmented using the "Isoline" drawing mode by creating a mask.

2.7.5. Behavioral tests

The Open Field Test (OFT) was used to evaluate emotional and ambulatory behavior. The OFT consisted of a square arena (40 × 40 × 30 cm^3) with dark PVC walls and a floor covered by sawdust and placed in dim illumination (light intensity 150 lx). The mice (*Ctrl, n* = 15; *Nex-cKO*, n = 15) were released in the corner of the arena and given 15 min to freely explore. The distance traveled over the arena and the central area and the time spent in the central area (20 × 20 cm^2) were recorded and analyzed using video tracking software. Time spent in the central area is usually considered as an index of anxiety under the assumption that the central area is more threatening for rodents than the peripheral area (Heredia et al., 2014). At the end of each experiment, sawdust was changed, and the apparatus was cleaned with 75% alcohol and dried before occupancy of the next mouse to avoid animal smells affecting the behavior test.

The Dark Light (DL) test was performed to investigate risk assessment and anxiety behaviors. The DL box consisted of an illuminated (30 × 20 cm^2) and a dark compartment (16 × 20 cm^2), separated by an opening. Mice (*Ctrl, n* = 13; *Nex-cKO*, n = 15) were placed at the center of the lit compartment (150 lx), and allowed free access between compartments for 10 min. The time spent in the light compartment, latency, and number of entries (considered when all four paws crossed the threshold) into the dark box were recorded.

The Forced Swimming Test (FST) is one of the most widely used tests across laboratories for assessing symptoms of depression. Mice (*Ctrl, n* = 8; *Nex-cKO*, n = 8) were individually placed in an inescapable transparent cylinder filled at 25 cm height of water (23–25 °C; 12 cm in diameter; 30 cm in height) for 6 min. The water depth was high enough to keep animals away from the bottom and from the walls. The immobility time of each animal during the last 4 min out of a total of 6 min was measured by a trained blind observer (Porsolt et al., 1977). Immobility was defined as the absence of movement, except for motion that was required to maintain the animal's head above the water. The water was changed after each trial.

Novelty-suppressed feeding. In this experiment, animals were food-deprived for 24 h before the test. Mice (*Ctrl, n* = 13; *Nex-cKO, n* = 14) were introduced into a brightly illuminated test environment (same arena used in open field) where a single food pellet was centrally placed on a small white paper for a 5 min session. In our protocol, the latency to reach the pellet (instead of the eating episode) was used as an index of induced anxiety-like behavior. Immediately after testing, mice were removed from the arena and placed into their home cage for 5 min, and food consumption was assessed.

Social Interaction test. In this paradigm, we measured social interest, which was defined as the approach and time that an experimental mouse spent with a novel mouse ("target mouse"). During a 5-min session, the mouse was introduced in an open field arena for free exploration. At the end of this initial exploration, the mouse was removed from the arena and two wired cages were placed into the arena (one empty, one with target mouse). The experimental mouse was then re-introduced in the arena for a 10-min session. The wire mesh cage allowed visual and olfactory interactions between mice but prevented direct physical contact. Time of interaction (in s) with the two cages and the locomotor activity of the experimental mouse were recorded and analyzed by the video tracking system. Number of mice used: *Ctrl, n* = 16; *Nex-cKO, n* = 14.

Social Dominance Tube test: Mice were tested as previously described by (Garfield et al., 2011) in a 30 cm long and 3 cm diameter tube. Testing was carried out in dimmed light conditions. Briefly, a wild-type and a mutant mouse of the same gender (which did not differ in weight by >10%) issued from the same home cage were placed at opposite ends of the tube and released. A subject was declared a "winner" when its opponent backed out of the tube. A $\chi 2$ one-sample analysis was used to determine if the number of wins by mutant animals was significantly different than chance. Number of mice used: *Ctrl*, n = 14; *Nex-cKO*, n = 14.

Skilled reaching-task. This test challenges mice for skilled voluntary movements. Adult mice (*Ctrl, n* = 8; *Nex-cKO, n* = 12) had to grasp food pellets through an indentation. Mice were first trained to reach food pellets with their forelimb paws through a 0.5 cm slit. The trial ended when 20 pellets were retrieved or 10 min passed. Before, mice were food-restricted to maintain 90% of their body weight. The training/test chamber was built from clear Plexiglas (1 mm thickness; dimensions 20 × 8.5 × 15 cm^3). One vertical slit (0.5-cm wide; 13-cm high) was located on the front wall of the box. Single reachable chocolate rice pellets were located outside the slit, on a platform of 1.5 cm height. After one day of habituation to the box without the presentation of pellets, rice pellets were presented inside the box to allow the mice to taste this food. During 5 training days, individual pellets were placed in front of the slit and mice were video-recorded. On test day, success rate was calculated as the percentage of successful reaches over total reaching attempts during the 5-min session (Percent Success = (number of successful retrievals)/ 100). Trials in which the mice used the tongue instead of the forelimb to retrieve the food pellet were not recorded. The data were analyzed using the video tracking software (Ethovision XT from Noldus Wageningen, The Netherlands). Behavioral assays were performed between 09:00 and 16:00. Mice were investigated by observers blinded for the genotype.

2.8. Units of measurement and statistical tests

In this study, the morphometric parameters measured (streamlines, volumes, thicknesses, and surfaces) are presented in absolute values (number, mm^3, µm, and mm^2, respectively) in the histograms of the figures and the tables. To facilitate the reading and understanding of the results, the variations in mutant mouse groups are expressed as a percentage relative to the control mouse group using the following formula: Δ-cKO% = ((cKO – mean Ctrl) / mean Ctrl) * 100. Two non-parametric tests are employed in our study. Either the Kruskal-Wallis test in the case of comparisons between the two mutant populations and the control population, or the Mann-Whitney test in the case of comparing two different populations. A difference between two populations is considered significant for a *p*-value <0.05. The mean values of absolute values and percentage variations are expressed ± the standard deviation (SD). The number of mice per group and the statistical tests used are indicated in the legends of the figures and tables. All statistical analyses are performed using Prism 9.0 software.

3. Results

3.1. Significant rearrangement of corpus callosum projections in Nr2f1 mouse mutants

The corpus callosum (cc) is the largest WM tract of the brain connecting the two cerebral hemispheres and facilitating communication

and coordination between them. The cc can be partitioned into distinct regions along the anteroposterior axis: the rostrum (including the lamina rostralis), the forceps minor of cc, which connects the lateral and medial surfaces of the frontal lobes and crosses the midline *via* the genu of cc, and the forceps major of the cc, which links the posterior portions of the occipital lobes with each other and crosses the midline *via* the splenium (Richards et al., 2004; Goldstein et al., 2023). Neuronal tracts
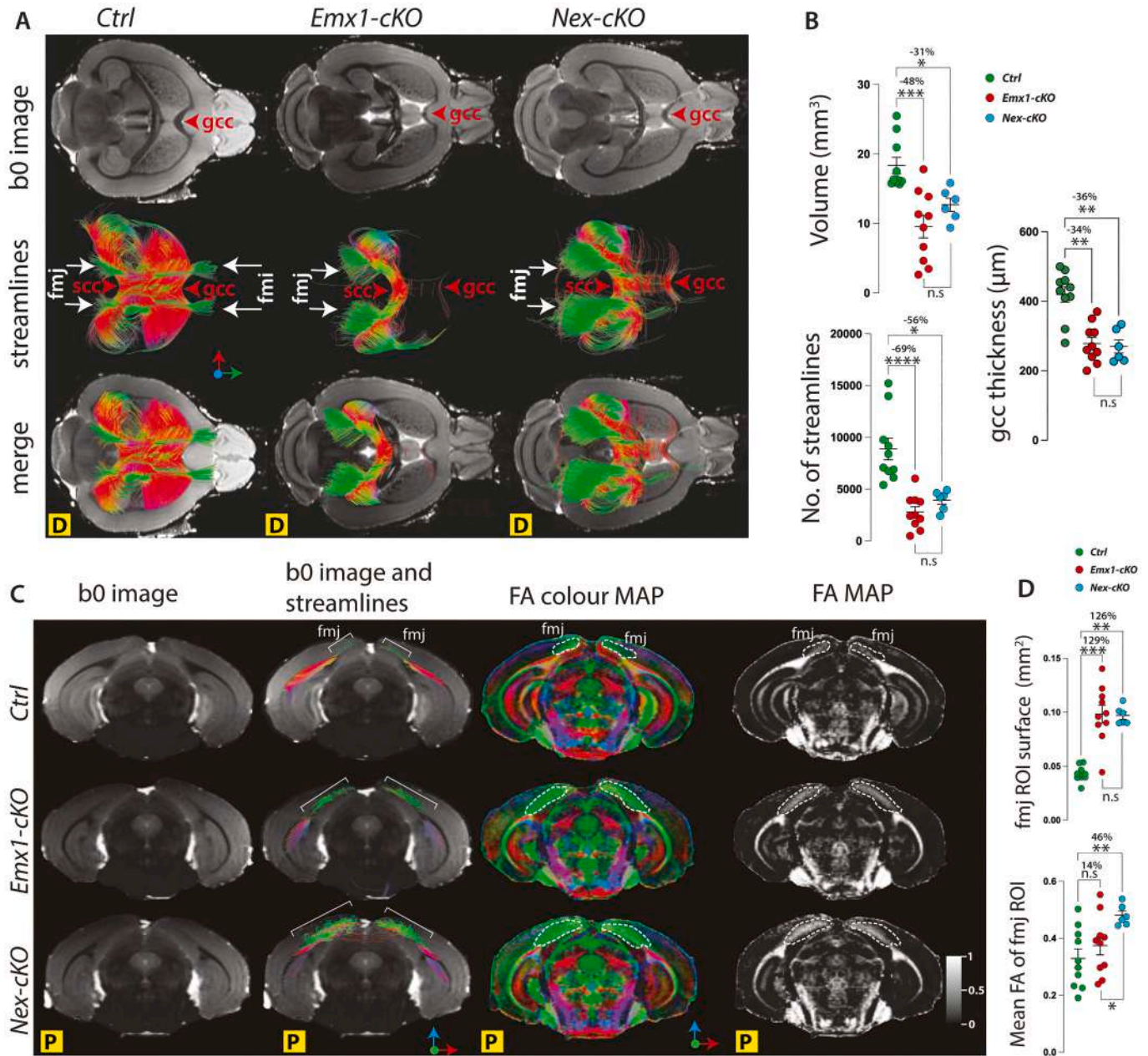
Fig. 1. Alterations and reorganization of the corpus callosum (cc) in conditional *knockout* mice. (A) 3D DTI tractography of the cc in control (*Ctrl*), *Emx1-cKO* and *Nex-cKO* mice. The color codes indicate WM fiber orientations are red in medial-lateral, blue in ventral-dorsal and green in rostral-caudal. Red arrows show the genus and the splenium of the cc (gcc and scc respectively). White arrows show the forceps major (fmj) and the forceps minor (fmi) of the cc projecting toward the frontal and the visual cortices, respectively. In both mutant mice, fmj projections are more abundant, while fmi projections are absent and the anterior part of the cc is drastically reduced. The letter D in yellow squares indicates dorsal views. (B) Graphical plots of the cc tract and the thickness of the gcc in *Ctrl* ($n = 10$), *Emx1-cKO* ($n = 10$) and *Nex-cKO* ($n = 6$) mice. Data represent the mean ± S·D; Kruskal-Wallis test; * $p < 0.05$; ** $p < 0.01$; *** $p < 0.001$; **** $p < 0.0001$. (C) Comparison of fmj projections between control (*Ctrl*) and mutant mice on coronal sections at Bregma - 4.04 mm. The codes of FA color maps show the spatial direction of the axons with medial-lateral (red), ventral-dorsal (blue), and rostral-caudal (green). The fmj tracts are shown under brackets and dashed lines indicate fmj ROIs that are drawn on FA color map and replicated on FA map. The letter P in yellow squares indicates posterior views. (D) Graphical plots of the area and the mean FA of fmj ROIs. Data represent the mean ± S·D.; Kruskal-Wallis test for the comparison of *Emx1-cKO* ($n = 10$) and *Nex-cKO* ($n = 6$) mutants with *Ctrl* ($n = 10$) mice. Mann-Whitney test for the comparison between *Emx1-cKO* and *Nex-cKO* mutants; n.s $p > 0.05$; *p < 0.01; ** p < 0.01; *** $p < 0.001$. Percentage changes between control and mutant mice are indicated. (For interpretation of the references to color in this figure legend, the reader is referred to the web version of this article.)

were reconstructed by DTI fiber tractography using a region of interest (ROI) type of approach (**Table S2**) (Gimenez et al., 2017).

3D DTI reconstructions of the cc showed a drastic reduction of the anterior two-thirds of the cc, including loss of the forceps minor (fmi) projections in both *Nr2f1* mutant mice (see white arrows in Fig. 1A). Accordingly, depletion of the anterior fiber tracts in mutant mice correlated with a thinner cc genu compared to *Ctrl* ones (Fig. 1A and B, anatomical b_0 reference images, gcc, *Emx1-cKO*: $-34 \pm 4\%$, $p = 0.0022$; *Nex-cKO*: $-36 \pm 5\%$, $p = 0.0058$). Strikingly, in both mutant mice, this anterior reduction was associated with hypertrophy of the posterior forceps minor (fmj) projections, strongly accentuated in *Nex-cKO* compared to *Ctrl* mice (Fig. 1A). Quantification in Fig. 1B confirmed a significant volume reduction (*Emx1-cKO*: $-48 \pm 8\%$, $p = 0.0006$; *Nex-cKO*: $-31 \pm 5\%$, $p = 0.02$) and reduction in the number of streamline fiber tracts forming the cc (*Emx1-cKO*: $-69 \pm 6\%$, $p < 0.0001$, *Nex-cKO*: $-56 \pm 4\%$, $p = 0.02$) in both *Nr2f1* mutant lines when compared to *Ctrl* mice. To further assess posterior changes in the cc, FA maps and color maps were used to delineate areas of the posterior fmj projections (Fig. 1C). The FA color maps graphically illustrate the direction of the fibers, enabling precise delineation of the fmj ROIs in the visual cortex (Fig. 1C, dash lines on FA color maps). The mean area of ROIs delineating fmj projections turned out to be significantly larger in both

mutants when compared to *Ctrl* (Fig. 1D; *Emx1-cKO*: $129 \pm 19\%$, $p = 0.0005$ and *Nex-cKO*: $126 \pm 6\%$, $p = 0.003$), suggesting a more ordered tract; however, the mean FA of the ROIs was found significant only in *Nex-cKO* mutant mice when compared to *Ctrl* ones (Fig. 1D; *Emx1-cKO*: $14 \pm 10\%$, $p = 0.79$ and *Nex-cKO*: $46 \pm 3\%$, $p = 0.0091$). Additionally, the mean fractional anisotropy (FA) of the ROIs is significantly higher in *Nex-cKO* compared to *Emx1-cKO* mice (Fig. 1D, two-tailed p-value = 0.0312, Mann-Whitney test). Altogether, these results indicate that the absence of *Nr2f1* in postmitotic neurons (*Nex-cKO*) induces a larger fmj phenotype.

Overall, distinct cc defects were observed in both models of *Nr2f1* mutant mice: a significant depletion of the anterior part of the cc with its volume reduction, a reshaping of the cc posterior part, and a fmj hypertrophy, which is particularly strong in *Nex-cKO* mice. The severe rerouting phenotype of the cc projections, from anterior to posterior underlines the major role of postmitotic *Nr2f1* in anteroposterior development of callosal projections neurons.

3.2. Hypertrophy and branching defects of the anterior commissure in Nr2f1 mutant mice

The anterior commissure (ac) is located ventral to the cc and to the
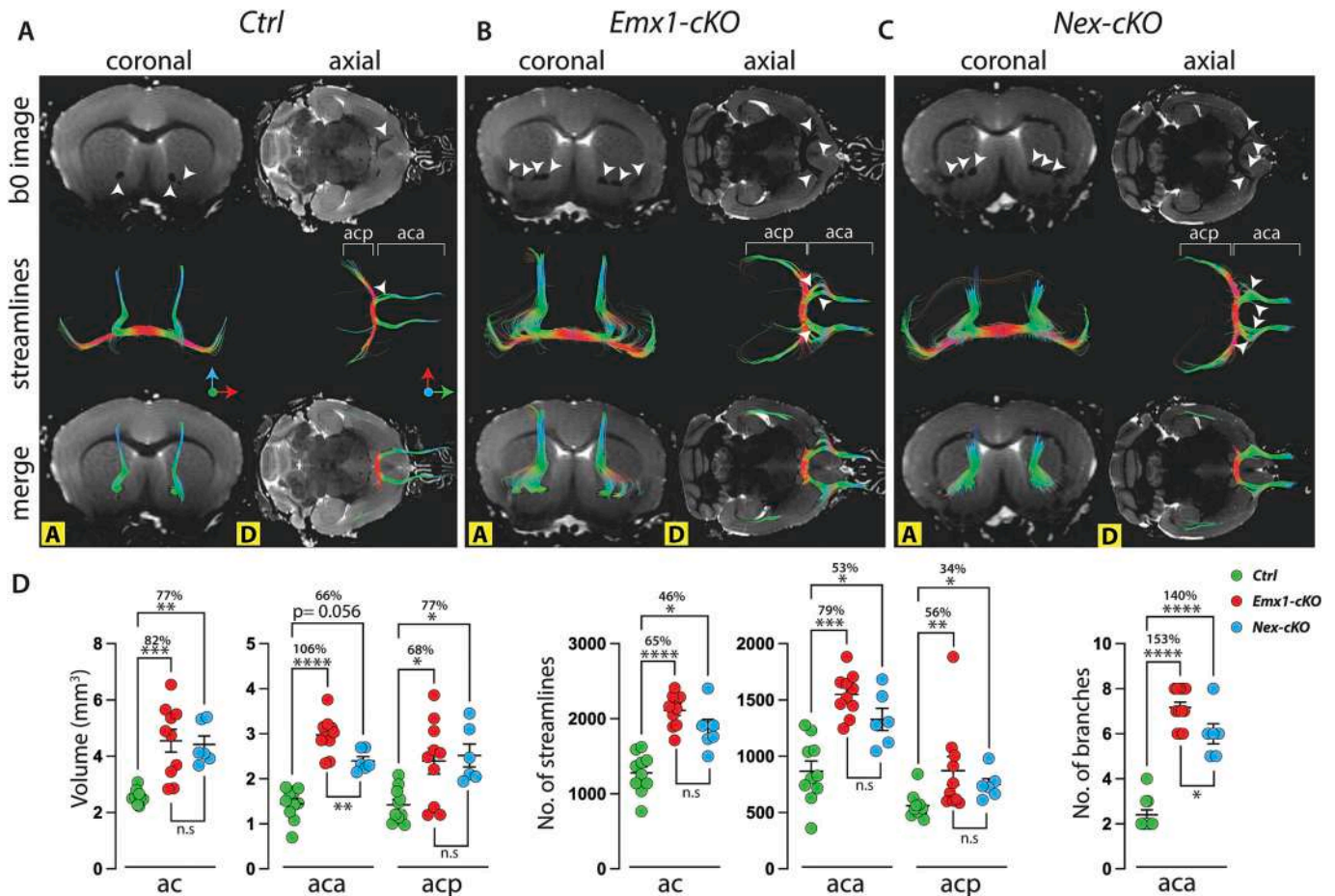
Fig. 2. Hypertrophy of the ac with an increased number of anterior branches in conditional *knockout* mice. (**A-C**) 3D DTI tractography reconstructions of the ac in control (*Ctrl*, A), *Emx1-cKO* (B) and *Nex-cKO* (C) mice. White arrowheads point to branches of the anterior part of the ac (aca). The aca in both *Emx1-cKO* and *Nex-cKO* is composed of multiple branches. The aca and the posterior part of the anterior commissures (acp) are indicated under brackets on axial planes. Tracts are colored according to their spatial direction with medial-lateral (red), ventral-dorsal (blue) and rostral-caudal (green) orientations. The letters A and D in yellow squares indicate anterior and posterior views, respectively. (**D**) Graphical plots of the ac, the aca and the acp and the number of branches of the aca in *Ctrl* ($n = 10$), *Emx1-cKO* ($n = 10$) and *Nex-cKO* ($n = 6$) mice. Data represent the mean ± S·D; Kruskal-Wallis test for the comparison of *Emx1-cKO* and *Nex-cKO* mutants with *Ctrl* mice. Mann-Whitney test for the comparison between *Emx1-cKO* and *Nex-cKO* mutants; n.s $p > 0.05$; * $p < 0.05$; ** $p < 0.01$; *** $p < 0.001$; **** $p < 0.0001$. Percentage changes between control and mutant mice are indicated. (For interpretation of the references to color in this figure legend, the reader is referred to the web version of this article.)

ventral hippocampal commissure and plays an important role in inter-hemispheric communication and coordination of brain functions. The ac is comprised of an anterior branch (aca), a horseshoe-shaped tract connecting the two olfactory bulbs, and a posterior one (acp) that forms a laterally directed tract entering into the external capsule and carrying projections between the two temporal lobes (Jouandet and Hartenstein, 1983).

Our 3D tractography reconstruction highlighted an enlargement of the entire ac tract in association with a higher number of branches forming the aca in both mutant mice compared to control (*Ctrl*) ones (Fig. 2A-C). The aca fragmentation into multiple branches is also visualized in the anatomical b_0 reference images (white arrowheads in Fig. 2A-C,) and was corroborated by a significant volume increase (ac, *Emx1-cKO*: 82 ± 15%, $p = 0.0004$ and *Nex-cKO*: 77 ± 11%, $p = 0.0032$) as well as component streamlines of the ac tract (ac, *Emx1-cKO*: 65 ± 5%, $p < 0.0001$ and *Nex-cKO*: 46 ± 9%, $p = 0.0232$; Fig. 2D) of mutant compared to *Ctrl* mice. This increase concerned both the anterior (aca volume, *Emx1-cKO*: 106 ± 9%, $p < 0.0001$ and *Nex-cKO*: 66 ± 6%, $p = 0.0564$; aca streamlines, *Emx1-cKO*: 79 ± 7%, $p = 0.0001$ and *Nex-cKO*: 53 ± 10%, $p = 0.0434$) and posterior parts of the ac (acp volume, *Emx1-cKO*: 68 ± 19%, $p = 0.0120$ and *Nex-cKO*: 77 ± 16%, $p = 0.0128$; acp streamlines, *Emx1-cKO*: 56 ± 21%, $p = 0.0047$ and *Nex-cKO*: 34 ± 8%, $p = 0.0169$). The increase in the volume of the anterior part of the aca is significantly more pronounced in *Emx1-cKO* mutants than in *Nex-cKO* mutants (Fig. 2D, two-tailed p-value = 0.0030, Mann-Whitney test). The number of branches forming the aca also increased significantly in both mutant (*Emx1-cKO*: 153 ± 11%, $p \leq 0.0001$ and *Nex-cKO*: 140 ± 16%, $p < 0.0001$) compared to *Ctrl* mice, but the average number of branches was significantly higher in *Emx1-cKO* than in *Nex-cKO* mice (Fig. 2D, Two-tailed p-value = 0.0324, Mann-Whitney test). Together, our results show an evident hypertrophy of the ac associated with an increased number of aca branches, which is particularly pronounced in mice in which *Nr2f1* function was abolished in progenitor cells (*Emx1-cKO*).

In support of the DTI data and with the aim to identify the cell populations at the origin of the ac disorganization in *Emx1-cKO* brains,

Nissl-positive neuronal cell bodies and Nissl-negative axonal tracts along the anteroposterior axis of the ventral brain were visualized and analyzed in histological coronal sections of adult mutant cortices (Fig. 3A). As expected, the surfaces areas of aca and acp and the number of aca branches, which appeared less compact and scattered, increased significantly in *Emx1-cKO* compared to *Ctrl* mice (aca surface, *Emx1-cKO*: 78 ± 34%, $p = 0,0043$; acp surface, *Emx1-cKO*: 164 ± 35%, p = 0,0043; aca branches, *Emx1-cKO*: 235 ± 30%, $p = 0,0022$) (Fig. 3B, C). Moreover, we found that the total surface area and length of the *Emx1-cKO* Pir were both significantly altered, particularly in its anterior part (APir), (56 ± 4%, $p = 0.0022$ and 25 ± 2%, $p = 0.0022$, respectively) when compared to the *Ctrl* counterparts (Fig. 3D).

The Pir is part of the paleocortex and is composed of three distinct layers (layers I to III) easily distinguishable in coronal sections due to the high density of Nissl-positive cells in layer II (Srinivasan and Stevens, 2018). Three morphometric parameters of layer II were analyzed, namely: surface area, fragmentation, and occupation percentage. Interestingly, the enlargement of the APir observed in the *Emx1-cKO* mutant was associated with a clear spatial disorganization of Nissl-positive cells in layer II (Fig. 4A). Moreover, compared to *Ctrl* mice, layer II of *Emx1-cKO* mice resulted expanded (95 ± 9%, $p = 0.0022$), fragmented (132 ± 26%, $p = 0.0022$), and occupied a larger territory within the APir (30 ± 7%, $p = 0.0043$) (Fig. 4B). These three parameters were not significantly altered in the PPir of *Emx1-cKO* mutant brains (Fig. 4B, p = 0.3939; $p = 0.4545$; p > 0,9999 respectively). Together, these histological data illustrate an abnormal distribution and organization of layer II neurons, particularly in the APir cortex, in line with an abnormally higher number of aca branches detected by 3D DTI tractography in *Emx1-cKO* compared to *Ctrl* brains.

3.3. Severe reduction in both major hippocampal tracts, the ventral hippocampal commissure, and the fornix, in Nr2f1 mutant mice

The hippocampus sends direct interhemispheric projections along the entire dorsoventral hippocampus *via* a structure called the ventral
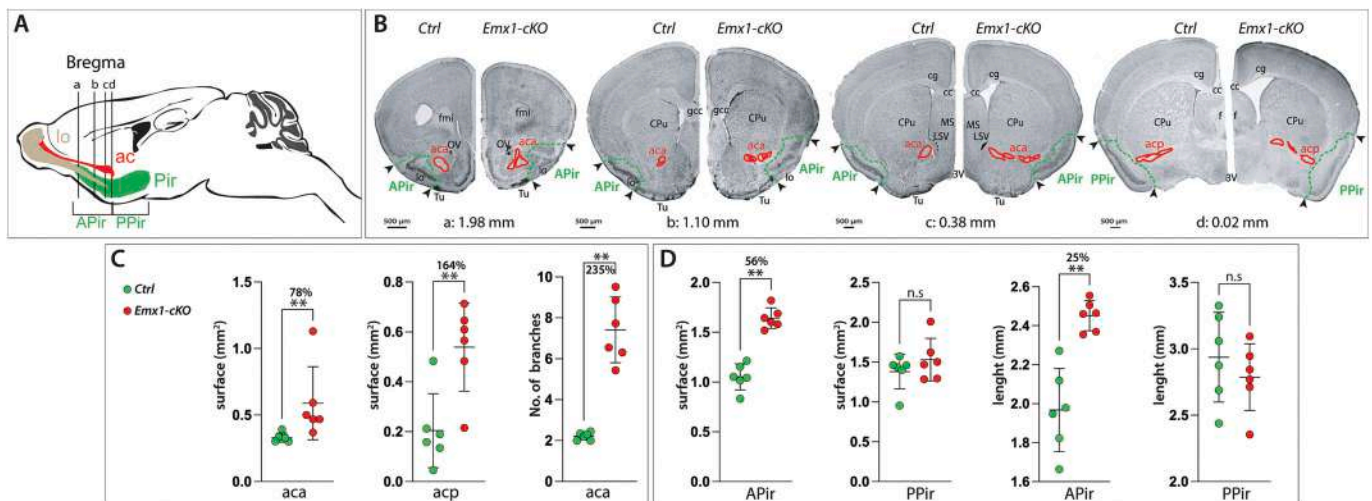
Fig. 3. Hypertrophy of the anterior commissure (ac) is associated with an enlargement of the anterior piriform cortex (APir) in *Emx1-cKO* mutant mice. (**A**) Sagittal diagram of mouse brain indicating the position relative to the Bregma of the four slices (a, b, c, and d) shown in B as well as the localization of the ac and the Pir represented in red and blue, respectively. The boundary between the anterior and posterior parts of the piriform cortex (APir and PPir, respectively) is defined by the disappearance of the lateral olfactory tract (lo). (**B**) Coronal half-sections of brains from control (*Ctrl*) and *Emx1-cKO* mice at the a, b, c, and d planes as indicated in A. The anterior commissures (aca and acp) and the APir and PPir are delineated by solid red and dashed green lines, respectively. The lengths of the APir and PPir correspond to the distance bordering the brain delimited by the two black arrowheads. Supplemental abbreviations: cc, corpus callosum; cg, cingulum; CPu, caudate putamen; f, fornix; fmi, forceps minor of the corpus callosum; gcc, genu of corpus callosum; lo, lateral optic tract; LSV, lateral septal nucleus, ventral part; MS, medial septal nucleus; OV, olfactory ventricle, Tu, olfactory tubercle; 3 V, 3rd ventricle. (**C**) Graphical plots of the means of the sum areas of aca and acp and of the average number of aca branches. (**D**) Graphical plots of the means of the sum areas and the means of the sum lengths of the APir and PPir. Control (*Ctrl*), n = 6 and *Emx1-cKO*, n = 6. Data represent the mean ± S·D; Mann-Whitney test; n.s $p > 0.05$, * $p < 0.05$, ** $p < 0.01$. Percentage changes between *Ctrl* and *Emx1-cKO* mice are indicated. (For interpretation of the references to color in this figure legend, the reader is referred to the web version of this article.)
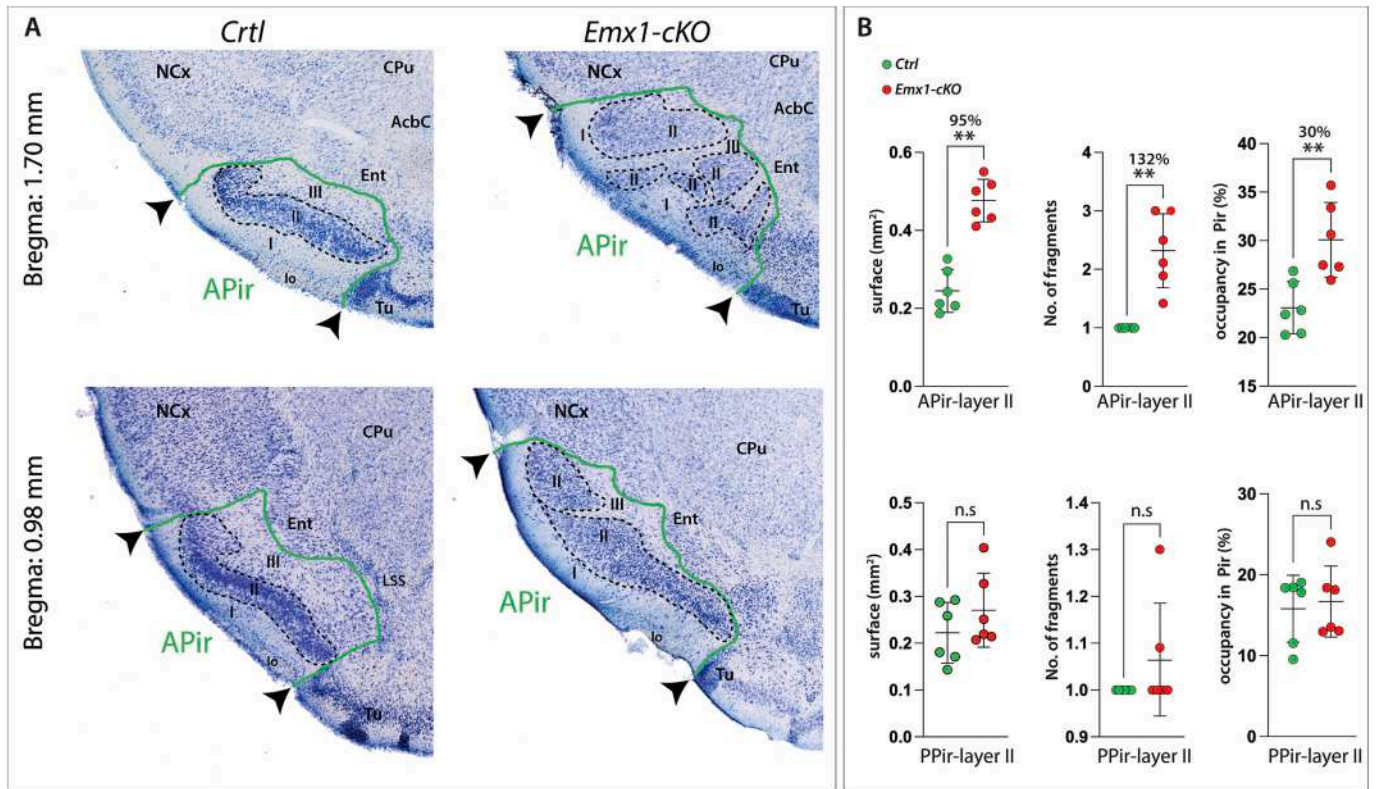
Fig. 4. Dramatic enlargement and fragmentation of layer II in the *Emx1-cKO* mutant anterior piriform cortex (APir). (**A**) Coronal views of the APir after cresyl violet staining of brain sections from control (*Ctrl*) and *Emx1-cKO* mice at Bregma 1.70 and 0.98 mm. The total surface of the APir is delineated by the solid green line, and layer II is delineated by the dashed black line. The locations of layer I and III of the APir, neocortex (NCx), entorhinal cortex (Ent), olfactory tubercle (Tu), nucleus accumbens core (AcbC), and caudate putamen (CPu) are indicated. (**B**) Graphical plots of the average surface, average length, and percentage of occupation of layer II in the APir or PPir cortex. *Ctrl*, $n = 6$ and *Emx1-cKO*, n = 6. Data are presented as mean ± S.D.; Mann-Whitney test; n.s $p > 0.05$, ** $p < 0.01$. Percentage changes between *Ctrl* and Emx1-cKO mutant mice are indicated. (For interpretation of the references to color in this figure legend, the reader is referred to the web version of this article.)
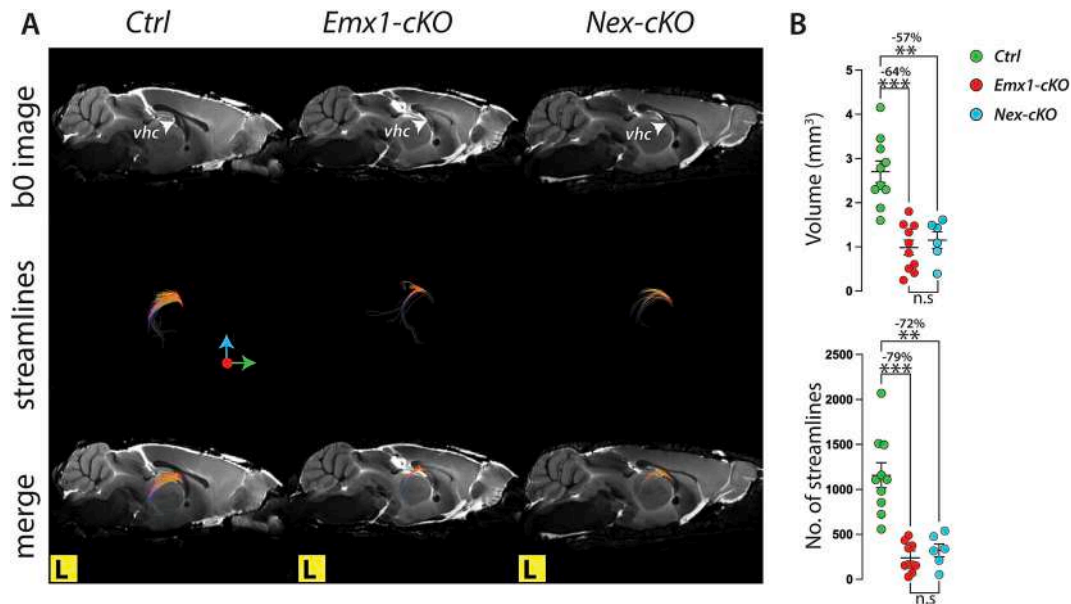
Fig. 5. Strong reduction of the ventral hippocampal commissure (vhc) in conditional *knockout* mice. (**A**) 3D DTI tractography reconstructions of the vhc in control (*Ctrl*), *Emx1-cKO* and *Nex-cKO* mice. The vhc is clearly visualized on anatomical b_0-reference images. The streamlines are colored according to their spatial direction with medial-lateral (red), ventral-dorsal (blue) and rostral-caudal (green) orientations. The letter L in yellow squares indicates lateral views. (**B**) Graphical plots of the number of streamlines and vhc tract volume in *Ctrl* ($n = 10$), *Emx1-cKO* (n = 10) and *Nex-cKO* ($n = 6$) animals. Data represent the mean ± S.D. Kruskal-Wallis test for the comparison of *Emx1-cKO* and *Nex-cKO* mutant with *Ctrl* mice. Mann-Whitney test for the comparison between *Emx1-cKO* and *Nex-cKO* mutants; n.s $p > 0.05$; ** $p < 0.01$; *** $p < 0.001$. Percentage changes between control and mutant mice are indicated. (For interpretation of the references to color in this figure legend, the reader is referred to the web version of this article.)

hippocampal commissure (vhc). Our 3D DTI tractography clearly shows a net reduction of the vhc tract in both *Nr2f1* mutant mice (Fig. 5A). Like the cc, the substantial reduction was also observed on the anatomical b_0-reference images (Fig. 5A, white arrowheads), and confirmed by a quantitative volume reduction (*Emx1-cKO*: - 64 ± 6%, $p = 0.0002$ and *Nex-cKO*: - 57 ± 6%, $p = 0.0065$) and streamline fiber tract numbers (*Emx1-cKO*: - 79 ± 4%, $p = 0.0001$ and *Nex-cKO*: - 72 ± 6%, $p = 0.0063$) in both mutant lines (Fig. 5B).

The fornix is a major hippocampal tract connecting the hippocampus to the hypothalamus and is composed of the alveus projection and of two major efferent tracts: the pre-commissural and the post-commissural fornix (pf). The pf is the major output of the hippocampus and is mainly composed of subicular axons that terminate in the mammillary bodies (Witter, 2006). Our 3D DTI reconstructions of the pf depicted as ventral views in Fig. 6A (pf, white arrowheads) displayed an unexpected abnormal shape in both mutant lines. However, we noticed a more severe reduction in *Emx1-cKO* than in *Nex-cKO* mutant brains since incomplete pf could only be observed in *Emx1-cKO* mice (Fig. 6, red arrowhead, 4/10 *Emx1-cKO* mice; 0/6 *Nex-cKO* mice). In comparison to *Ctrl* mice, the number of streamline fiber tracts (Fig. 6B, *Emx1-cKO*: - 50 ± 3%, $p < 0.0001$ and *Nex-cKO*: - 37 ± 4%, $p = 0.0506$), as well as the volume of the pf (Fig. 6B, *Emx1-cKO*: - 58 ± 9%, $p = 0.0017$ and *Nex-cKO*: - 58 ± 6%, $p = 0.0222$), were reduced in both mutant lines. Furthermore, the severe reduction in the number of streamlines was associated with a significant decrease in their average length, suggesting substantial structural deterioration of this neural bundle in mutant brains (**Table S3**; *Emx1-cKO*: −42 ± 8%, $p = 0.0029$ and *Nex-cKO*: −36 ± 7%, $p = 0.0052$) when compared to the *Ctrl* counterparts. Together, our results demonstrate a significant reduction and defects of the two major hippocampal efferent tracts, namely the pf and the vhc, particularly in the *Emx1-cKO* mutant brain.

In addition to DTI, we used fluorescent microscopy of cleared brains to measure the volumetric alterations of the pf in the *Nex-cKO* mouse strain expressing the eYFP protein under the control of the *Thy-1* promoter (Feng et al., 2000; Porrero et al., 2010) (**Fig. S1A**). In this mouse strain, eYFP protein is strongly expressed in the hippocampal formation,

including the subiculum, which is the main axonal source of the pf. Segmentation of the pf in cleared brains revealed a similar volumetric decrease as that measured by 3D DTI tractography (**Fig. S1B**; −40 ± 9%, $p = 0.0303$), and validate our microscopic 3D DTI tractography method developed for *ex vivo* brain imaging.

3.4. No morphometric abnormalities in other brain tracts of Nr2f1 mutants

In light of the severe abnormalities observed in the major brain commissures (cc, ac, vhc and pf) in the absence of *Nr2f1*, we wondered whether other important tracts involved in cognitive and emotional behaviors were also affected in *Nr2f1* mutant brains. We thus analyzed the integrity of the fasciculus retroflexus (fr), the main efferent tract of the habenula involved in the regulation of the reward system and the modulation of emotional and motivational behaviors (Roman et al., 2020), the mammillothalamic tract (mt) connecting the mammillary bodies and the thalamus, playing crucial roles in the circuitry of the limbic system involved in emotion, memory, and spatial navigation and the stria medullaris (sm), which connects the habenular nuclei with the limbic system (Roman et al., 2020). We did not find any significant changes in the volumes, number of streamline tract fibers, or the morphological appearance of these neuronal tracts in either *Emx1-cKO* or *Nex-cKO* brains when compared to their *Ctrl* counterparts (**Fig. S2A–D**).

Finally, we analyzed other WM structures that have been described as potentially affected in *Nr2f1null* or *cKO* mice. The pyramidal tract (py) connects the motor cortex to the spinal cord and is located ventrally between the pons and the spinal cord. In accordance with our previous work (Tomassy et al., 2010), no obvious differences in this tract were reported from our 3D DTI analysis (**Fig. S3A–D**). The optic tract (opt), which transmits visual stimuli from the neural retina to the thalamus, and the stria terminalis (st), which connects the amygdala to the hypothalamus, were also not affected by the absence of cortical *Nr2f1* expression. However, the average length of streamline fiber tracts in the stria terminalis was significantly reduced in the *Nex-cKO* but not *Emx1-*
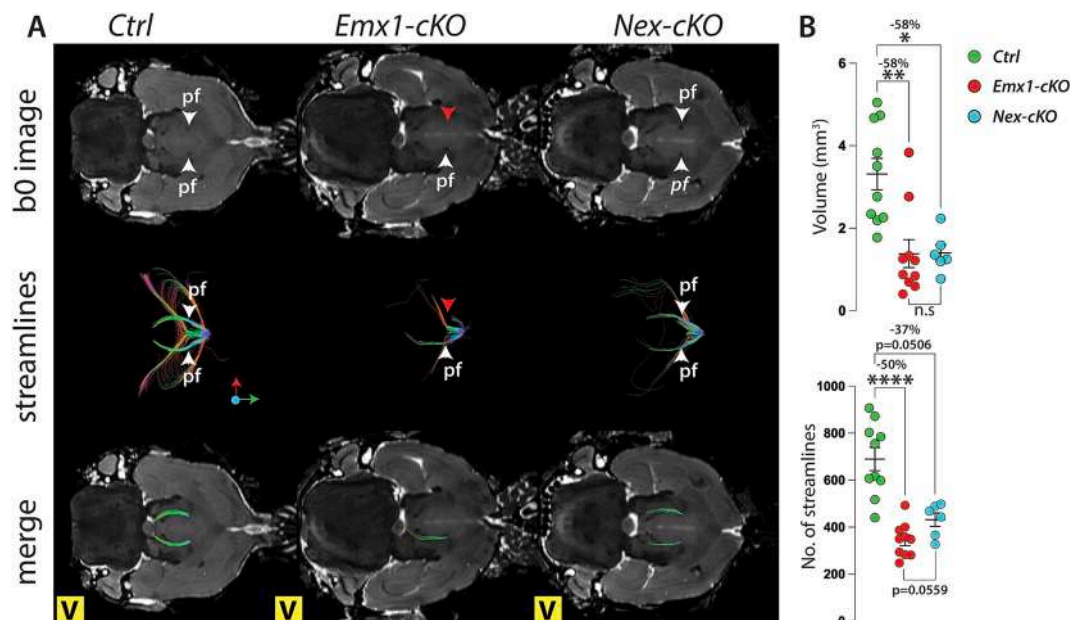
Fig. 6. **Reduction and alterations of post-commissural fornices (pf) in conditional *knockout* mice.** (**A**) 3D DTI tractography reconstructions of the pf in control (*Ctrl*), *Emx1-cKO* and *Nex-cKO* mice. White arrowheads point to the pf tract and the red to the truncated one in the *Emx1-cKO* mouse. Streamline color-coded orientations are indicated. The letter V in yellow squares indicates ventral views. (**B**) Graphical plots of the number of streamlines and pf volume in *Ctrl* (n = 10), *Emx1-cKO* (n = 10) and *Nex-cKO* (n = 6) animals. Data represent the mean ± S.D. Kruskal-Wallis test for the comparison of *Emx1-cKO* and *Nex-cKO* mutants with *Ctrl* mice. Mann-Whitney test for the comparison between *Emx1-cKO* and *Nex-cKO* mutants; n.s $p > 0.05$; ** $p < 0.01$; **** $p < 0.0001$. Percentage changes between control and mutant mice are indicated. (For interpretation of the references to color in this figure legend, the reader is referred to the web version of this article.)

cKO mutants when compared to *Ctrls* (**Table S4**; *Nex-cKO*: $-10 \pm 3\%$, $p = 0.022$). Since the *Cre-recombinase* is also expressed in the amygdalar nuclei of *Nex-Cre* mice (Goebbels et al., 2006), our results suggest a possible modification of these regions in *Nex-cKO* mutant mice.

3.5. Imapired locomotor and social dominance behaviors in Nex-cKO mice

Our data have depicted a strong phenotype in several major brain commissures in both *Nr2f1* mutant mice. Since these commissures together with the fornix are known to influence several cognitive functions, we wondered whether these aspects were altered in adult *Nex-cKO* mutant mice, which were never tested for behavioral features. We thus challenged these mice for performances in the Open Field Test (OFT, for locomotion and anxiety), in the Dark-Light box (DL, for risk assessment and anxiety), in the Novelty-Suppressed Feeding test (NSFT, for induced anxiety-like behavior), in the Forced Swimming Test (FST, for symptoms of depression), in the Social Interaction and Dominance Tube Tests (for social interactions) and in the Skilled Reaching-Task (for voluntary skilled movements).

Our data (Fig. 7) display an increased locomotor activity of *Nex-cKO* mutant compared to control (*Ctrl*) mice when assessed for exploratory activity in an open field apparatus during 15-min sessions (total distance traveled in cm) (*Ctrl*: $n = 15$, mean $= 5290 \pm 300$; *Nex-cKO*: n $= 15$, mean $= 6687 \pm 509$, $p = 0.04$) (Fig. 7A). Despite this hyperactivity, *Nex-cKO* mice performed well in the skilled reaching task when they needed to catch food pellets through an indentation with their paws (percentage of success) (*Ctrl*: $n = 8$, mean $= 22.7\% \pm 3.9$; *Nex-cKO*: $n = 12$, mean $= 19.8\% \pm 2.2$, $p = 0.5$) (Fig. 7B), indicating that mutant mice have no particular problems in the coordination and planning of voluntary movements.

To assess anxiety-like behaviors, we used different behavioral tests, such as the OFT, the DL box, and the Novelty-suppressed Feeding tests (Fig. 7C-E). During the OFT, the percentage of time spent in the central area (as an index of anxiety) showed no significant changes between controls and mutants (time in s spent in the central zone) (*Ctrl*: n $= 15$, mean $= 89 \pm 9.9$; *Nex-cKO*: n $= 15$, mean $= 88 \pm 12.5$, $p = 0.9$) (Fig. 7C). Similarly, the time spent in the lighted compartment of the DL box showed no significant difference between the two experimental groups (*Ctrl*: $n = 13$, mean $= 181 \pm 18$; *Nex-cKO*: n $= 15$, mean $= 230 \pm 20$, $p = 0.28$) (Fig. 7D). In the NSFT, food-deprived mice were tested for their motivation of hunger against the tendency to avoid the center of an open field chamber in brightly lit conditions. Anxiogenic-related behavior was determined by the time latency for mice to reach and eat the pellet (Santarelli et al., 2003). Again, no statistical differences were observed between controls and *Nex-cKO* mice in the time necessary to reach the pellet in the central zone (*Ctrl*: n $= 13$, mean $= 66.4 \pm 23$; *Nex-cKO*: $n = 14$, mean $= 61.7 \pm 17$, $p = 0.59$) (Fig. 7E). Together, these three independent tests assess that *Nex-cKO* mice are no more no less anxious than control littermates.

Next, we assessed depression-like behaviors and levels of resignation by testing control and mutant littermates in the FST. In this task, the time spent floating in the cylinder filled with water is considered immobile (immobility time) and evaluated as a sign of resignation. Statistical analysis showed no differences between groups for the time of immobility (*Ctrl*: n $= 8$, mean $= 147.4 \pm 24$; *Nex-cKO*: n $= 8$ mean $= 176.7 \pm 15$, $p = 0.49$) (Fig. 7F), suggesting no depressive-like behavior in *Nex-cKO* mice.

Finally, to test social features, we first used the social interaction test and social novelty preference (Moy et al., 2004). Both groups (*Ctrl* and *Nex-cKO* mice) spent a significantly longer time around the wire cage with the stranger mouse than the empty cage, strongly indicating a preference for social novelty, and statistical analysis supported no difference between groups for the distance traveled in the apparatus during the 5 min habituation session (*Ctrl*: n $= 16$, mean $= 2021 \pm 152$; *Nex-cKO*: n $= 14$, mean $= 1857 \pm 200$, $p = 0.33$) and during the 10 min test
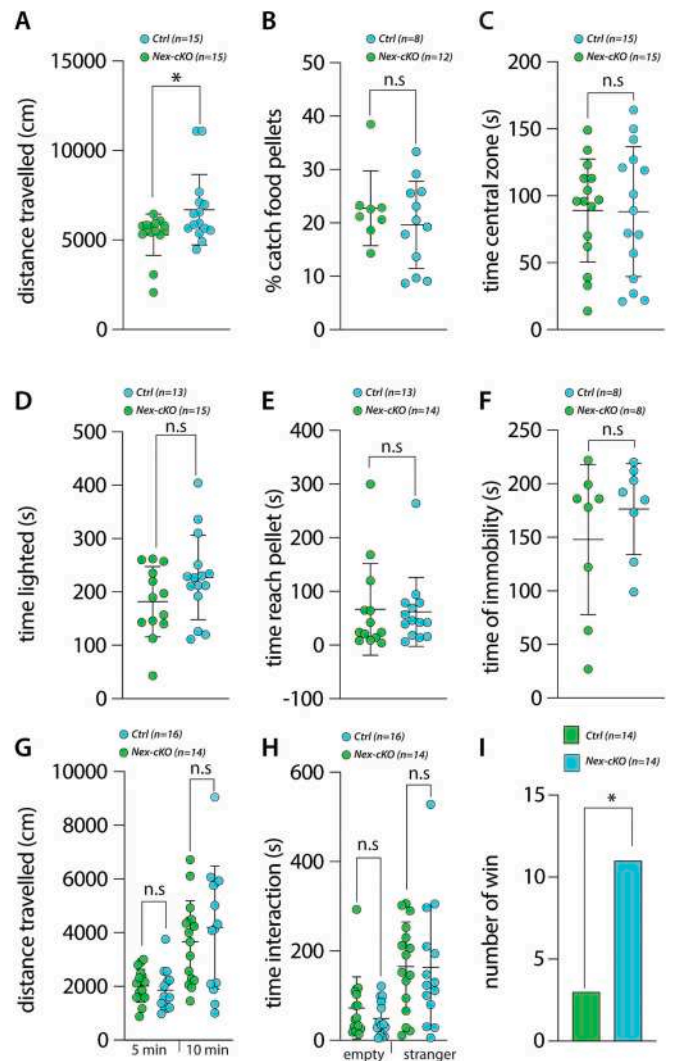
Fig. 7. Behavioral studies of *Nex-cKO* mutant mice. (A) Mouse locomotor activity was assessed using an open field test. Mutant mice expressed significant hyperactivity compared to the control group. (B) Voluntary movement coordination was not affected in the skilled reaching task. Anxiety-like behavior was evaluated by mouse performance in the open-field task (time spent in the central zone) (C), in the dark-light test (D), and in the novelty-suppressed feeding task (by recording the time to reach the pellet) (E). Depressive-like behavior was assessed using the forced swim test (F). During the sociability tests, graphs show the total distance traveled (G) and the time of interaction (H) in the whole arena during the habituation and the test sessions. In the tube test, the number of victories was significantly higher in the *Nex-cKO* compared to the control group (I). The number of mice for each test is indicated. Data represent the mean $\pm$ SD. Mann-Whitney test; n.s $p > 0.05$; * $p < 0.05$.

session (*Ctrl*: n $= 16$, mean $= 3663 \pm 381$; *Nex-cKO* n $= 14$, mean $= 4191 \pm 613$, $p = 0.72$) (Fig. 7G). During the test session, the time spent exploring the empty cage (*Ctrl*: n $= 16$, mean $= 72 \pm 17$; *Nex-cKO*: n $= 14$, mean $= 48 \pm 10$, $p = 0.31$) and the cage containing the stranger mouse (*Ctrl*: n $= 16$, mean $= 165 \pm 25$; *Nex-cKO* n $= 14$, mean $= 163 \pm 37$, $p = 0.64$) showed that both groups spent statistically more time exploring the cage with the mouse than the empty one ($F(1;28) = 18.5$, $p = 0.002$) (Fig. 7H). Finally, we used the social dominance or tube test, in which two mice compete for passage in a narrow tube (Lindzey et al., 1961; Wang et al., 2011; Fan et al., 2019). Successful performance in a tube test is often associated with a dominant status in rodents (Lindzey et al., 1961). Our data show that when mutant mice were paired with a familiar, weight-matched control littermate mouse, the *Nex-cKO* animals won significantly more encounters (statistical analysis (11/14), $\chi 2$

$= 4.84$, $p = 0.02$) (Fig. 7I), suggesting a dominant-type social behavior in *Nex-cKO* mutant mice.

Collectively, our data show that *Nex-cKO* mice are hyperactive, but not particularly anxious or depressed, well perform fine skilled movements, are interested in social interactions but tend to show a more dominant type of social behavior than their control littermates.

4. Discussion

4.1. μ-3D DTI acquisition visualize major mouse brain tracts

We used μ-3D DTI-validated method (Gimenez et al., 2017) to visualize the major tract of the mouse brain *ex vivo*. The method was designed to reach a high spatial resolution in an acceptable scan time and to avoid imaging artefacts that could compromise accurate quantification of fiber tract changes. We used spin-echo RF sequence with Cartesian k-space rather than the rapid EPI sequence to avoid ghost artefacts. We put the number of gradient orientations to its lower limit to reduce scan timing, favoring spatial resolution but also to minimize motion artefacts that can occur from rapid switching at each diffusion gradient orientation. Thanks to the properties of the paramagnetic Gd-based CAs injected into mice during PFA perfusion, T_1 relaxation time was decreased by about 20 times allowing the use of a very short repetition time that accelerated MRI scan without SNR penalty. Here for the first time, DTI tractography was applied to *Nr2f1* conditional mouse mutants and our methodology was accurate to reconstruct major WM tract, identify tract defects, and successfully compare *Emx1-cKO* and *Nex-cKO* mutants to control mice. Importantly, this method allowing tract reconstruction was validated by histology and by fluorescent microscopy of cleared brains.

All these tractography outcomes reinforced our knowledge about *Nr2f1* functional role in WM development, guiding us in emitting novel hypotheses and emphasizing us to study subtle WM tract connectivity in the future. This cannot be achieved from the present data but rather by using new protocols of high angular resolution diffusion imaging (HARDI) (Alomair et al., 2015; Anderson et al., 2020). Indeed, valuable efforts have been recently made by our group to increase imaging speed either by using compressed sensing (de Souza et al., 2023) or by using the Super Resolution Reconstruction post-processing method (Gimenez et al., 2023), both with the goal to increase angular resolution in diffusion imaging that is now largely recognized powerful in fundamental studies to detect impairment of WM integrity and connectivity on animal models of neurological diseases.

4.2. The impact of interhemispheric connections in Nr2f1 mouse models

Interhemispheric communication *via* axonal connections between the left and right hemispheres of the brain has been highly conserved during evolution and plays a crucial role in the bilateral integration of various sensory, motor, and cognitive functions. In the context of NDDs, disruptions in these interhemispheric connections can have significant implications for brain function and behavior. This is why it is crucial to understand the genetic origin and specific nature of interhemispheric connectivity disruptions that will ultimately affect the assembly and functioning of the neuronal network. It is well accepted that proper development of brain commissures requires a sequence of complex processes involving area patterning, cell-type specification, guidance cues, axonal growth, and navigation, as well as activity-dependent establishment of contralateral connections. In humans, malfunctioning of these events at any stage of development can prevent the normal formation of these commissures, resulting in mild to severe sensory-motor and cognitive conditions, characteristic of NDDs (Paul et al., 2007; Suarez et al., 2014).

4.3. Abnormal shape and connectivity of the corpus callosum (cc) in Nr2f1 mutant mice and BBSOAS patients

The most common commissural abnormality described by MRI in human patients comprises agenesis (absence) or hypoplasia (underdevelopment) of the cc, which will lead to various emotional and social impairments (Paul et al., 2007; Schell-Apacik et al., 2008). For example, social situations can require rapid processing of very complex information (*i.e.,* lexical and affective processes) that is typically handled within lateralized regions and may be particularly sensitive to cc abnormality (Paul et al., 2007).

Regarding BBSOAS, around 70–80% of patients show callosal abnormalities of different degrees, as reported by neuroimaging analyses (Chen et al., 2016; Bertacchi et al., 2020; Desai et al., 2023). These morphological defects resulted quite heterogeneous with normal or decreased anteroposterior callosal length and segmental thinning and/or thickening (Bertacchi et al., 2020; Desai et al., 2023). Our previous 2D histological analysis on *Nr2f1 Emx1-cKO* adult mutants described an overall 30% to 40% reduction of the anteroposterior extension and total volume of the callosal commissure (Alfano et al., 2011); however, a detailed morphological and quantitative 3D analysis of the different portions of the cc was lacking. Here, we show a strong volumetric reduction of the anterior part of the cc tract (genu and fmi fibers) associated with a striking reshaping and hypertrophy of the posterior splenium and fmj projections (Fig. 1). Several issues might explain this strong phenotype. On one hand, we can envisage a rerouting phenotype of anterior to posterior cc projections associated with an abnormal motor to somatosensory areal organization (Alfano et al., 2014); on the other hand, tangential and radial expansion of the occipital cortex (Bertacchi et al., 2020) might lead to an overproduction of callosal projections, particularly after birth, when the posterior splenium shows higher growth rates than those of the anterior genu (Ren et al., 2006). However, since the cc defects result more severe in *Nex-cKO* than in *Emx1-cKO* mice, *i.e.,* in the absence of *Nr2f1* expression in post-mitotic neurons, we propose that the re-wiring process might happen in *Nr2f1*-deficient callosal neurons; these neurons might be less responsive to guidance cues, which are necessary to segregate anterior from posterior projections. The semaphorin3A/neuropilin-1 signaling might be a potential candidate pathway controlled by post-mitotic *Nr2f1*, since the anterior to posterior axonal segregation within the cc was highly disturbed upon disruption of this pathway (Zhou et al., 2013), ultimately resulting in intermixing between dorsal and ventral callosal axons, a phenotype that we also observed in *Nr2f1 null* fetuses (Armentano et al., 2006). Thus, the morphological heterogeneity of the cc abnormalities observed in BBSOAS patients might depend on the impact of individual pathogenic mutations on the modulation of this and/or other guidance signaling pathways.

4.4. Interdependence between the corpus callosum (cc) and the ventral hippocampal commissure (vhc)

Our tractography data show that besides the cc, the vhc located ventrally to the cc was also strongly reduced in *Emx1-cKO* and *Nex-cKO* mutant mice. Even if they both cross the dorsal midline, the two commissures innervate different contralateral targets: the cc allows proper communication between somatotopic areas of the neocortex, whereas the vhc is a smaller commissural pathway interconnecting ventral parts of the hippocampus. They also serve distinct functions: the cc is mainly required in language processing, perception, memory, and problem-solving, while the hippocampus is a crucial structure involved in learning, memory, and spatial navigation. Although the cc and vhc acquire distinct morphologies and functions, the two structures form very closely during mid-stage brain development and seem to depend on each other. Several studies (including MRI) have shown that the cc is anchored early in development, anteriorly by the lamina rostralis region, which is the first region to develop, and posteriorly by the fornix/

hippocampal commissure (Ren et al., 2006). However, developmental studies in rodents suggest that while the first callosal axons crossing the midline anteriorly use pioneer axons from the cingulate cortex, in more posterior regions, these axons grow close to the ones of the hippocampal commissure, which forms one day earlier (Richards et al., 2004). This implies a tight correlation between callosal axons crossing the midline and the formation of the hippocampus and its commissure. Our previous studies revealed a strong dysmorphic hippocampus with altered shape, volume, and connectivity in *Emx1-cKO* (and to a lesser extent in *Nex-cKO*) adult brains (Flore et al., 2017; Parisot et al., 2017). It is thus possible that the malformed dorsal hippocampus in mutant mice influence the formation and trajectories of both commissures and that callosal and hippocampal axons find an abnormal substrate on which to migrate, and/or simply an alternative route.

4.5. Laminar and axonal disorganization of the piriform cortex (Pir) and anterior commissure (ac)

Besides abnormalities in the cc, our study highlights morphological defects of the ac and Pir in *Nr2f1* mutant mice. The ac has a more evolutionary ancient origin than the cc and has the function of connecting olfactory and amygdaloid regions already in lower vertebrates. The ac conveys connections to diverse brain areas through three major routes: (i) the anterior branch carries fibers from the anterior olfactory nucleus to the contralateral olfactory bulb, (ii) the posterior branch connects the Pir, lateral entorhinal cortex, and temporal association areas, and (iii) the stria terminalis branch carries fibers from the cortical amygdala and nucleus of the lateral olfactory tract (Fenlon et al., 2021). Our data clearly show a hypertrophic ac, including enlarged posterior and anterior branches, together with an increased number of anterior branches in both *Nr2f1* mutant mice. Interestingly, this phenotype was more severe in the *Emx1-cKO* line than the *Nex-cKO* line (Fig. 2), and 2D histological analysis in *Emx1-cKO* brains confirmed scattered axonal ac branches and an abnormally laminar organization of the Pir (Fig. 3). Indeed, differently from the neocortex, the Pir is composed of three layers, characteristic of paleocortical regions, whereby layer II is populated with a compact mix of principal cells (Mazo et al., 2017). Interestingly, our histological study shows high laminar disorganization of layer II neurons in *Emx1-cKO* mutants, particularly in the APir, the largest region of the primary olfactory cortex and the primary site for the initial processing of odor identity encoding and association (Wang et al., 2020).

The Pir is considered a primary olfactory cortex by receiving direct inputs from the olfactory bulb and sending projections to various other brain regions, such as the amygdala, the orbitofrontal and entorhinal cortex, which play a significant role in the emotional and cognitive evaluation of olfactory information and processing (Wang et al., 2020). Its functions include odor discrimination, olfactory learning and memory, pattern recognition, and integration with higher brain regions, contributing to the ability to perceive and interpret a wide range of smells in the environment and thus influencing emotion, memory, and social behavior (Bekkers and Suzuki, 2013). Because of these key cognitive functions, it is not surprising, that the Pir is implicated in various neurological disorders, such as epilepsy and ASD (Wang et al., 2020). Our previous study reported high expression of *Nr2f1* in the Pir and associated structures (Armentano et al., 2006) and showed that loss of *Nr2f1* in the *Emx1* lineage affected the maintenance of the dopaminergic phenotype in the olfactory bulb *via* an activity-dependent mechanism (Bovetti et al., 2013). This highlights a key role for *Nr2f1* in the control of sensory-dependent plasticity in peripheral olfactory processing. Nothing is known about how this would influence central olfactory encoding, but the abnormal organization of the Pir described in this study might suggest that this is the case.

4.6. Mitotic versus post-mitotic role of Nr2f1 in the development of interhemispheric connections

The sequential development of the different commissures seems to follow the evolutionary path, whereby the ac forms first, followed by the hippocampal commissure and then the cc (Ashwell et al., 1996). Thus, development might follow a basic configuration and a general plan upon which evolution can act. Localized patterning centers, that secrete a conserved set of morphogens able to specify cellular fate, have been proposed to shape the formation of telencephalic commissures along the dorsoventral axis (Suarez et al., 2014). The commissural plate is located at the anterior telencephalic midline and expresses the fibroblast growth factor FGF8, which provides positional information to cells by regulating the expression of a whole series of patterning factors, among which *Nr2f1*. Appropriate FGF8 signaling is necessary for the correct development of neurons that will form the first commissures (anterior, posterior and hippocampal) and also serves as a guidance cue for growing axons (Shanmugalingam et al., 2000; Tole et al., 2006; Zhang et al., 2023). Disruptions in FGF8 signaling can lead to abnormalities in the formation of commissures, which may result in neurodevelopmental disorders (Sapir et al., 2022). Since FGF8 acts very early in establishing *Nr2f1* gradient expression in progenitor cells (Garel et al., 2003; Terrigno et al., 2018), it is thus reasonable to expect that loss of *Nr2f1*, one of the major FGF8 effector genes, will affect the formation of the commissures originating in the commissural plate. This is particularly evident for the ac (Fig. 2), the most ancient forebrain commissure, that resulted highly affected upon loss of *Nr2f1* in progenitors ((Armentano et al., 2006) and this study).

Moreover, the hippocampal plate originates from a restricted area in the medial cortical neuroepithelium, called DGN (Dentate Gyrus Neuroepithelium), highly expressing *Nr2f1 and* patterned by secreted morphogens in the hem. While mitotic deletion of *Nr2f1* leads to severe morphogenetic defects resulting in a dysmorphic hippocampus with altered shape, volume, and connectivity (Flore et al., 2017; Parisot et al., 2017), postmitotic *Nr2f1* inactivation leads to milder defects (Parisot et al., 2017), suggesting that initial formation of the hippocampal primordium is mainly under the influence of *Nr2f1* in neural progenitor cells. However, our study also shows that the vhc and the fornix were strongly affected in both mutants, even if *Emx1-cKO* brains tended to be slightly more severe than *Nex-cKO* ones (Figs. 5,6). This implies that post-mitotic *Nr2f1* expression does play an important role in commissural formation independently from *Nr2f1* mitotic expression. We propose that *Nr2f1* expressed in neuronal cells refines cell-type specification and axon guidance of developing tracts. Consistently, we reported no obvious differences in areal organization, neocortical laminar specification, and thalamocortical axonal projections between *Emx1-cKO* and *Nex-CKO* cortices (Alfano et al., 2014). Hence, specification cues from post-mitotic neurons will further refine a nascent developmental program and drive neurons toward their final identity and target structures (reviewed in (Bonnefont and Vanderhaeghen, 2021). This also implies that the final specification of cortical neurons can still be influenced at postmitotic stages, in line with our observation of similar tract defects (apart from the ac see above) in *Emx1-cKO* and *Nex-cKO* brains.

4.7. Abnormal interhemispheric connections and disease progression

Disruptions in the neuronal pathways that connect different regions of the two hemispheres of the brain will lead to a range of symptoms and conditions and contribute to the development of NDDs, including BBSOAS. However, because the major interhemispheric connections were altered in *Nr2f1* mutants, it becomes very difficult to attribute associated functional deficits to the absence of one specific commissure. Abnormalities in the cc, that we observed in mutant mice and in BBSOAS patients, could lead to intellectual disabilities, attention deficits, difficulties in fine motor coordination, and social interactions (Paul et al., 2007). These anatomical defects and cognitive disabilities are well-

represented in patients and partially reproduced in *Nr2f1* conditional mice, although with variable severities. For example, skilled motor behaviors involving fine motor coordination were affected in *Emx1-cKO* mice (Tomassy et al., 2010), reproducing an apraxia phenotype in BBSOAS patients (Chen et al., 2016; Bertacchi et al., 2022). However, this was not the case for *Nex-cKO* mutants despite the strong cc wiring defects (this study), suggesting that abnormal fine skilled movements are most probably caused by other connectivity defects than abnormal cc wiring, consistent with our previous study (Tocco et al., 2022).

On the other hand, we report that *Nr2f1* loss-of-function in cortical postmitotic neurons can influence social behavior. Social cognition and interactions represent a sensitive domain in NDDs, and social dominance is a critical factor for the maintenance of a stable social structure in animals. The compartmental tube test was originally developed to test dominance hierarchies in mice (Lindzey et al., 1961). In this study, we show that *Nr2f1 Nex-cKO* mutants won over littermate controls and acted dominantly (Fig. 7I), a type of social behavior that was never reported before in studies dealing with *Nr2f1* mutant mice (Contesse et al., 2019; Zhang et al., 2020). Previous work showed that social dominance is governed by many neurotransmitters, such as dopamine (Jupp et al., 2016) and additional brain systems (Wang et al., 2011). Notably, the increased social dominance phenotype observed in the *Nex-cKO* mice is highly similar to mouse models for monogenic forms of ASD, including *Shank2* (Han et al., 2020) or *Fmr1* mouse models (de Esch et al., 2015; Zeidler et al., 2018). Increased winning in the tube test may reproduce an inability to recognize the social status of conspecifics. Surprisingly, we did not detect any differences in the social approach or social preference as assessed in the three-chamber test, which was instead altered in a mouse model with a dominant-negative point mutation (Zhang et al., 2020). This is however in line with other mouse models of ASD where normal social approach behaviors are not affected (Molosh et al., 2014; Papale et al., 2017). As suggested by (Borrie et al., 2021), the tube test paradigm measures a more complex social scenario compared to the three-chamber test since mice meet multiple conspecifics separately, developing and maintaining a hierarchical relationship over time.

Interestingly, we found that both mutant mice, the *Emx1-cKO,* and the *Nex-cKO*, show a higher spontaneous locomotor activity ((Contesse et al., 2019) and this study), consistent with a hyperactivity phenotype and often associated with Attention Deficit Hyperactivity Disorder (ADHD), whose features have been diagnosed in 20–30% of BBSOAS patients (Chen et al., 2016; Bertacchi et al., 2022). ADHD symptoms are often associated with widespread brain macro- and microstructural abnormalities, as revealed by MRI studies, and among the affected cortical circuits, the limbic system seems to contribute to the presence of emotional and cognitive disturbances, as well as excessive and impulsive behavior in young ADHD adults (Davenport et al., 2010; Gehricke et al., 2017). Here, we show a severe volume reduction and an altered shape of the post-commissural tract (pf) of the fornix in both *Nr2f1* mutant lines (Fig. 6). The pf belongs to a group of limbic connections involved in memory, emotion, motivation, and spatial navigation (Bubb et al., 2017), and its disruption is associated with deficiencies in attention, impulse control, and executive functions (Koshiyama et al., 2020). *Nr2f1* mutant mice have impaired spatial learning and memory combined with altered hippocampal synaptic plasticity (Flore et al., 2017; Chen et al., 2020), as well as hyperactive features and anxiolytic-like behaviors when compared to their littermate controls (Contesse et al., 2019). A similar pf phenotype has been described in mouse mutants deficient for the microtubule-associated protein 6 (MAP6), whose dysregulation has been associated with a schizophrenic-like phenotype (Deloulme et al., 2015; Gimenez et al., 2017; Cuveillier et al., 2021). Interestingly, an automated yeast two-hybrid screening has shown a strong binding between MAP6 and Nr2f1 proteins (Albers et al., 2005), suggesting that both factors might interact during the development of the post-commissural fornix pathway. Moreover, semaphorin 3E controls the development and guidance of the pf (Chauvet et al., 2007) and MAP6 is an important effector in this signaling pathway (Deloulme et al., 2015).

Hence, similar to the cc, the semaphorin-neuropilin signaling might represent a convergent pathway controlling formation and guidance of several commissural systems downstream of *Nr2f1*.

5. Conclusions

Thanks to the use of the 3D DTI WM tractography, reinforced by 3D fluorescent imaging and 2D histology, we were able to unveil severe interhemispheric commissural connectivity defects in two adult BBSOAS mouse models. The advantage of using these two mouse lines, in which *Nr2f1* is solely inactivated in the cortex, relies on the fact that any morphological and/or tract defects can be specifically reported as abnormalities intrinsic to the neocortex, paleocortex and/or archicortex. These include piriform and entorhinal cortex, but also hippocampal and amygdala regions, where *Nr2f1* is highly expressed. In addition, these mouse lines are viable until adulthood, thus allowing an overall characterization at adult stages that can be correlated to behavior. We have shown that 3D DTI tractography has helped investigate the specific impact of loss of *Nr2f1* on morphometry and quantitative WM microstructures and established relevant relationships with some brain structures and functions; these can be further analyzed by cellular, molecular, and behavioral means. Overall, our study highlights the importance of generating different mouse disease models to help relate the precise impact of the loss of the gene during early development, in adulthood. Finally, this preclinical study clearly shows the interest of 3D DTI to provide relevant morphometric biomarkers for a more detailed diagnosis in BBSOAS patients, since diffusion MRI has the unique advantage of reconstructing and studying WM tracts of the whole brain non-invasively.

CRediT authorship contribution statement

Jean Christophe Deloulme: Writing – review & editing, Writing – original draft, Visualization, Validation, Supervision, Resources, Methodology, Formal analysis, Data curation, Conceptualization. **Maxime Leclercq:** Validation, Resources, Methodology, Formal analysis, Data curation. **Olivier Deschaux:** Writing – review & editing, Visualization, Validation, Supervision, Methodology, Formal analysis, Data curation, Conceptualization. **Gemma Flore:** Writing – review & editing, Visualization, Validation, Methodology, Formal analysis, Data curation. **Laetitia Capellano:** Methodology, Investigation, Data curation. **Chiara Tocco:** Resources, Methodology. **Barbara Yael Braz:** Data curation, Formal analysis. **Michèle Studer:** Writing – review & editing, Writing – original draft, Visualization, Validation, Supervision, Resources, Project administration, Investigation, Funding acquisition, Formal analysis, Data curation, Conceptualization. **Hana Lahrech:** Writing – review & editing, Validation, Supervision, Resources, Methodology, Funding acquisition, Formal analysis, Data curation, Conceptualization.

Declaration of competing interest

The authors declare that they have no conflict of interest.

Data availability

Data will be made available on request.

Appendix A. Supplementary data

Supplementary data to this article can be found online at https://doi.org/10.1016/j.nbd.2024.106455.

References

Albers, M., Kranz, H., Kober, I., Kaiser, C., Klink, M., Suckow, J., Kern, R., Koegl, M., 2005. Automated yeast two-hybrid screening for nuclear receptor-interacting proteins. Mol. Cell. Proteomics 4, 205–213.

Alexander, A.L., Lee, J.E., Lazar, M., Field, A.S., 2007. Diffusion tensor imaging of the brain. Neurotherapeutics 4, 316–329.

Alfano, C., Viola, L., Heng, J.I., Pirozzi, M., Clarkson, M., Flore, G., De Maio, A., Schedl, A., Guillemot, F., Studer, M., 2011. COUP-TFI promotes radial migration and proper morphology of callosal projection neurons by repressing Rnd2 expression. Development 138, 4685–4697.

Alfano, C., Magrinelli, E., Harb, K., Hevner, R.F., Studer, M., 2014. Postmitotic control of sensory area specification during neocortical development. Nat. Commun. 5, 5632.

Alomair, O.I., Brereton, I.M., Smith, M.T., Galloway, G.J., Kurniawan, N.D., 2015. In vivo high angular resolution diffusion-weighted imaging of mouse brain at 16.4 tesla. PLoS One 10, e0130133.

Anderson, R.J., Long, C.M., Calabrese, E.D., Robertson, S.H., Johnson, G.A., Cofer, G.P., O'Brien, R.J., Badea, A., 2020. Optimizing diffusion imaging protocols for structural connectomics in mouse models of neurological conditions. Front. Phys. 8.

Armentano, M., Filosa, A., Andolfi, G., Studer, M., 2006. COUP-TFI is required for the formation of commissural projections in the forebrain by regulating axonal growth. Development 133, 4151–4162.

Armentano, M., Chou, S.J., Tomassy, G.S., Leingartner, A., O'Leary, D.D., Studer, M., 2007. COUP-TFI regulates the balance of cortical patterning between frontal/motor and sensory areas. Nat. Neurosci. 10, 1277–1286.

Ashwell, K.W., Marotte, L.R., Li, L., Waite, P.M., 1996. Anterior commissure of the wallaby (Macropus eugenii): adult morphology and development. J. Comp. Neurol. 366, 478–494.

Bekkers, J.M., Suzuki, N., 2013. Neurons and circuits for odor processing in the piriform cortex. Trends Neurosci. 36, 429–438.

Bertacchi, M., Romano, A.L., Loubat, A., Tran Mau-Them, F., Willems, M., Faivre, L., Khau van Kien, P., Perrin, L., Devillard, F., Sorlin, A., et al., 2020. NR2F1 regulates regional progenitor dynamics in the mouse neocortex and cortical gyrification in BBSOAS patients. EMBO J. 39, e104163.

Bertacchi, M., Tocco, C., Schaaf, C.P., Studer, M., 2022. Pathophysiological heterogeneity of the BBSOA neurodevelopmental syndrome. Cells 11.

Billiet, B., Amati-Bonneau, P., Desquiret-Dumas, V., Guehlouz, K., Milea, D., Gohier, P., Lenaers, G., Mirebeau-Prunier, D., den Dunnen, J.T., Reynier, P., et al., 2022. NR2F1 database: 112 variants and 84 patients support refining the clinical synopsis of Bosch-Boonstra optic atrophy syndrome. Hum. Mutat. 43, 128–142.

Bonnefont, J., Vanderhaeghen, P., 2021. Neuronal fate acquisition and specification: time for a change. Curr. Opin. Neurobiol. 66, 195–204.

Borrie, S.C., Plasschaert, E., Callaerts-Vegh, Z., Yoshimura, A., D'Hooge, R., Elgersma, Y., Kushner, S.A., Legius, E., Brems, H., 2021. MEK inhibition ameliorates social behavior phenotypes in a Spred1 knockout mouse model for RASopathy disorders. Mol. Autism. 12, 53.

Bosch, D.G., Boonstra, F.N., Gonzaga-Jauregui, C., Xu, M., de Ligt, J., Jhangiani, S., Wiszniewski, W., Muzny, D.M., Yntema, H.G., Pfundt, R., et al., 2014. NR2F1 mutations cause optic atrophy with intellectual disability. Am. J. Hum. Genet. 94, 303–309.

Boulan, B., Ravanello, C., Peyrel, A., Bosc, C., Delphin, C., Appaix, F., Denarier, E., Kraut, A., Jacquier-Sarlin, M., Fournier, A., et al., 2021. CRMP4-mediated fornix development involves Semaphorin-3E signaling pathway. eLife 10.

Bovetti, S., Bonzano, S., Garzotto, D., Giannelli, S.G., Iannielli, A., Armentano, M., Studer, M., De Marchis, S., 2013. COUP-TFI controls activity-dependent tyrosine hydroxylase expression in adult dopaminergic olfactory bulb interneurons. Development 140, 4850–4859.

Bubb, E.J., Kinnavane, L., Aggleton, J.P., 2017. Hippocampal - diencephalic - cingulate networks for memory and emotion: an anatomical guide. Brain Neurosci Adv 1.

Calamante, F., 2017. Track-weighted imaging methods: extracting information from a streamlines tractogram. MAGMA 30, 317–335.

Chauvet, S., Cohen, S., Yoshida, Y., Fekrane, L., Livet, J., Gayet, O., Segu, L., Buhot, M.C., Jessell, T.M., Henderson, C.E., et al., 2007. Gating of Sema3E/PlexinD1 signaling by neuropilin-1 switches axonal repulsion to attraction during brain development. Neuron 56, 807–822.

Chen, C.A., Bosch, D.G., Cho, M.T., Rosenfeld, J.A., Shinawi, M., Lewis, R.A., Mann, J., Jayakar, P., Payne, K., Walsh, L., et al., 2016. The expanding clinical phenotype of Bosch-Boonstra-Schaaf optic atrophy syndrome: 20 new cases and possible genotype-phenotype correlations. Genet Med. 18 (11), 1143–1150.

Chen, C.A., Wang, W., Pedersen, S.E., Raman, A., Seymour, M.L., Ruiz, F.R., Xia, A., van der Heijden, M.E., Wang, L., Yin, J., et al., 2020. Nr2f1 heterozygous knockout mice recapitulate neurological phenotypes of Bosch-Boonstra-Schaaf optic atrophy syndrome and show impaired hippocampal synaptic plasticity. Hum. Mol. Genet. 29, 705–715.

Chou, S.J., Babot, Z., Leingartner, A., Studer, M., Nakagawa, Y., O'Leary, D.D., 2013. Geniculocortical input drives genetic distinctions between primary and higher-order visual areas. Science 340, 1239–1242.

Contesse, T., Ayrault, M., Mantegazza, M., Studer, M., Deschaux, O., 2019. Hyperactive and anxiolytic-like behaviors result from loss of COUP-TFI/Nr2f1 in the mouse cortex. Genes Brain Behav. e12556.

Cuveillier, C., Boulan, B., Ravanello, C., Denarier, E., Deloulme, J.C., Gory-Faure, S., Delphin, C., Bosc, C., Arnal, I., Andrieux, A., 2021. Beyond neuronal microtubule stabilization: MAP6 and CRMPS, two converging stories. Front. Mol. Neurosci. 14, 665693.

Davenport, N.D., Karatekin, C., White, T., Lim, K.O., 2010. Differential fractional anisotropy abnormalities in adolescents with ADHD or schizophrenia. Psychiatry Res. 181, 193–198.

de Esch, C.E., van den Berg, W.E., Buijsen, R.A., Jaafar, I.A., Nieuwenhuizen-Bakker, I. M., Gasparini, F., Kushner, S.A., Willemsen, R., 2015. Fragile X mice have robust mGluR5-dependent alterations of social behaviour in the Automated Tube Test. Neurobiol. Dis. 75, 31–39.

de Souza, D.A.R., Mathieu, H., Deloulme, J.C., Barbier, E.L., 2023. Evaluation of kernel low-rank compressed sensing in preclinical diffusion magnetic resonance imaging. Front. Neurosci. 17, 1172830.

Deloulme, J.C., Gory-Faure, S., Mauconduit, F., Chauvet, S., Jonckheere, J., Boulan, B., Mire, E., Xue, J., Jany, M., Maucler, C., et al., 2015. Microtubule-associated protein 6 mediates neuronal connectivity through Semaphorin 3E-dependent signalling for axonal growth. Nat. Commun. 6, 7246.

Desai, N.K., Kralik, S.F., Edmond, J.C., Shah, V., Huisman, T., Rech, M., Schaaf, C.P., 2023. Common neuroimaging findings in Bosch-Boonstra-Schaaf optic atrophy syndrome. AJNR Am. J. Neuroradiol. 44, 212–217.

Fan, Z., Zhu, H., Zhou, T., Wang, S., Wu, Y., Hu, H., 2019. Using the tube test to measure social hierarchy in mice. Nat. Protoc. 14, 819–831.

Feng, G., Mellor, R.H., Bernstein, M., Keller-Peck, C., Nguyen, Q.T., Wallace, M., Nerbonne, J.M., Lichtman, J.W., Sanes, J.R., 2000. Imaging neuronal subsets in transgenic mice expressing multiple spectral variants of GFP. Neuron 28, 41–51.

Fenlon, L.R., Suarez, R., Lynton, Z., Richards, L.J., 2021. The evolution, formation and connectivity of the anterior commissure. Semin. Cell Dev. Biol. 118, 50–59.

Fillard, P., Toussaint, N., 2006. Medical image navigation and research tool by INRIA (MedINRIA). Enseignement 1–39.

Flore, G., Di Ruberto, G., Parisot, J., Sannino, S., Russo, F., Illingworth, E.A., Studer, M., De Leonibus, E., 2017. Gradient COUP-TFI expression is required for functional Organization of the Hippocampal Septo-Temporal Longitudinal Axis. Cereb. Cortex 27, 1629–1643.

Franklin, B.J. Keith, Paxinos, G., 2008. The Mouse Brain in Stereotaxic Coordinates, Compact: The Coronal Plates and Diagrams. Elsevier Science.

Garel, S., Huffman, K.J., Rubenstein, J.L., 2003. Molecular regionalization of the neocortex is disrupted in Fgf8 hypomorphic mutants. Development 130, 1903–1914.

Garfield, A.S., Cowley, M., Smith, F.M., Moorwood, K., Stewart-Cox, J.E., Gilroy, K., Baker, S., Xia, J., Dalley, J.W., Hurst, L.D., et al., 2011. Distinct physiological and behavioural functions for parental alleles of imprinted Grb10. Nature 469, 534–538.

Gehricke, J.G., Kruggel, F., Thampipop, T., Alejo, S.D., Tatos, E., Fallon, J., Muftuler, L. T., 2017. The brain anatomy of attention-deficit/hyperactivity disorder in young adults - a magnetic resonance imaging study. PLoS One 12, e0175433.

Gimenez, U., Perles-Barbacaru, A.T., Millet, A., Appaix, F., El-Atifi, M., Pernet-Gallay, K., van der Sanden, B., Berger, F., Lahrech, H., 2016. Microscopic DTI accurately identifies early glioma cell migration: correlation with multimodal imaging in a new glioma stem cell model. NMR Biomed. 29, 1553–1562.

Gimenez, U., Boulan, B., Mauconduit, F., Taurel, F., Leclercq, M., Denarier, E., Brocard, J., Gory-Faure, S., Andrieux, A., Lahrech, H., et al., 2017. 3D imaging of the brain morphology and connectivity defects in a model of psychiatric disorders: MAP6-KO mice. Sci. Rep. 7, 10308.

Gimenez, U., Deloulme, J.C., Lahrech, H., 2023. Rapid microscopic 3D-diffusion tensor imaging fiber-tracking of mouse brain in vivo by super resolution reconstruction: validation on MAP6-KO mouse model. MAGMA 36, 577–587.

Goebbels, S, Bormuth, I, Bode, U, Hermanson, O, Schwab, MH, Nave, KA, 2006. Genetic targeting of principal neurons in neocortex and hippocampus of NEX-Cre mice. Genesis 44, 611–621.

Goldstein, A., Covington, B.P., Mahabadi, N., Mesfin, F.B., 2023. Neuroanatomy, Corpus Callosum. In: StatPearls. StatPearls Publishing Copyright © 2023, StatPearls Publishing LLC, Treasure Island (FL).

Han, K.A., Yoon, T.H., Shin, J., Um, J.W., Ko, J., 2020. Differentially altered social dominance- and cooperative-like behaviors in Shank2- and Shank3-mutant mice. Mol. Autism. 11, 87.

Heredia, L., Torrente, M., Colomina, M.T., Domingo, J.L., 2014. Assessing anxiety in C57BL/6J mice: a pharmacological characterization of the open-field and light/dark tests. J. Pharmacol. Toxicol. Methods 69, 108–114.

Jiang, Y., Johnson, G.A., 2010. Microscopic diffusion tensor imaging of the mouse brain. Neuroimage 50, 465–471.

Jouandet, M.L., Hartenstein, V., 1983. Basal telencephalic origins of the anterior commissure of the rat. Exp. Brain Res. 50, 183–192.

Jupp, B., Murray, J.E., Jordan, E.R., Xia, J., Fluharty, M., Shrestha, S., Robbins, T.W., Dalley, J.W., 2016. Social dominance in rats: effects on cocaine self-administration, novelty reactivity and dopamine receptor binding and content in the striatum. Psychopharmacology 233, 579–589.

Koshiyama, D., Fukunaga, M., Okada, N., Morita, K., Nemoto, K., Usui, K., Yamamori, H., Yasuda, Y., Fujimoto, M., Kudo, N., et al., 2020. White matter microstructural alterations across four major psychiatric disorders: mega-analysis study in 2937 individuals. Mol. Psychiatry 25, 883–895.

Lindzey, G., Winston, H., Manosevitz, M., 1961. Social dominance in inbred mouse strains. Nature 191, 474–476.

Loscher, W., Ebert, U., 1996. The role of the piriform cortex in kindling. Prog. Neurobiol. 50, 427–481.

Mazo, C., Grimaud, J., Shima, Y., Murthy, V.N., Lau, C.G., 2017. Distinct projection patterns of different classes of layer 2 principal neurons in the olfactory cortex. Sci. Rep. 7, 8282.

Molosh, A.I., Johnson, P.L., Spence, J.P., Arendt, D., Federici, L.M., Bernabe, C., Janasik, S.P., Segu, Z.M., Khanna, R., Goswami, C., et al., 2014. Social learning and amygdala disruptions in Nf1 mice are rescued by blocking p21-activated kinase. Nat. Neurosci. 17, 1583–1590.

Moy, S.S., Nadler, J.J., Perez, A., Barbaro, R.P., Johns, J.M., Magnuson, T.R., Piven, J., Crawley, J.N., 2004. Sociability and preference for social novelty in five inbred strains: an approach to assess autistic-like behavior in mice. Genes Brain Behav. 3, 287–302.

Neville, K.R., Haberly, L.B., 2004. Olfactory Cortex. Oxford University Press, New York, NY.

O'Connell, S., Cannon, D.M., Broin, P.O., 2023. Predictive modelling of brain disorders with magnetic resonance imaging: a systematic review of modelling practices, transparency, and interpretability in the use of convolutional neural networks. Hum Brain Mapp. 44 (18), 6561–6574.

Papale, A., d'Isa, R., Menna, E., Cerovic, M., Solari, N., Hardingham, N., Cambiaghi, M., Cursi, M., Barbacid, M., Leocani, L., et al., 2017. Severe intellectual disability and enhanced gamma-aminobutyric acidergic synaptogenesis in a novel model of rare RASopathies. Biol. Psychiatry 81, 179–192.

Parisot, J., Flore, G., Bertacchi, M., Studer, M., 2017. COUP-TFI mitotically regulates production and migration of dentate granule cells and modulates hippocampal Cxcr4 expression. Development 144, 2045–2058.

Paul, L.K., Brown, W.S., Adolphs, R., Tyszka, J.M., Richards, L.J., Mukherjee, P., Sherr, E. H., 2007. Agenesis of the corpus callosum: genetic, developmental and functional aspects of connectivity. Nat. Rev. Neurosci. 8, 287–299.

Porrero, C., Rubio-Garrido, P., Avendano, C., Clasca, F., 2010. Mapping of fluorescent protein-expressing neurons and axon pathways in adult and developing Thy1-eYFP-H transgenic mice. Brain Res. 1345, 59–72.

Porsolt, R.D., Le Pichon, M., Jalfre, M., 1977. Depression: a new animal model sensitive to antidepressant treatments. Nature 266, 730–732.

Rech, M.E., McCarthy, J.M., Chen, C.A., Edmond, J.C., Shah, V.S., Bosch, D.G.M., Berry, G.T., Williams, L., Madan-Kheterpal, S., Niyazov, D., et al., 2020. Phenotypic expansion of Bosch-Boonstra-Schaaf optic atrophy syndrome and further evidence for genotype-phenotype correlations. Am. J. Med. Genet. A 182, 1426–1437.

Ren, T., Anderson, A., Shen, W.B., Huang, H., Plachez, C., Zhang, J., Mori, S., Kinsman, S. L., Richards, L.J., 2006. Imaging, anatomical, and molecular analysis of callosal formation in the developing human fetal brain. Anat Rec A Discov Mol Cell Evol Biol 288, 191–204.

Richards, L.J., Plachez, C., Ren, T., 2004. Mechanisms regulating the development of the corpus callosum and its agenesis in mouse and human. Clin. Genet. 66, 276–289.

Roman, E., Weininger, J., Lim, B., Roman, M., Barry, D., Tierney, P., O'Hanlon, E., Levins, K., O'Keane, V., Roddy, D., 2020. Untangling the dorsal diencephalic

conduction system: a review of structure and function of the stria medullaris, habenula and fasciculus retroflexus. Brain Struct. Funct. 225, 1437–1458.

Santarelli, L., Saxe, M., Gross, C., Surget, A., Battaglia, F., Dulawa, S., Weisstaub, N., Lee, J., Duman, R., Arancio, O., et al., 2003. Requirement of hippocampal neurogenesis for the behavioral effects of antidepressants. Science 301, 805–809.

Sapir, T., Sela-Donenfeld, D., Karlinski, M., Reiner, O., 2022. Brain organization and human diseases. Cells 11.

Schell-Apacik, C.C., Wagner, K., Bihler, M., Ertl-Wagner, B., Heinrich, U., Klopocki, E., Kalscheuer, V.M., Muenke, M., von Voss, H., 2008. Agenesis and dysgenesis of the corpus callosum: clinical, genetic and neuroimaging findings in a series of 41 patients. Am. J. Med. Genet. A 146A, 2501–2511.

Schneider, C.A., Rasband, W.S., Eliceiri, K.W., 2012. NIH image to ImageJ: 25 years of image analysis. Nat. Methods 9, 671–675.

Shanmugalingam, S., Houart, C., Picker, A., Reifers, F., Macdonald, R., Barth, A., Griffin, K., Brand, M., Wilson, S.W., 2000. Ace/Fgf8 is required for forebrain commissure formation and patterning of the telencephalon. Development 127, 2549–2561.

Srinivasan, S., Stevens, C.F., 2018. The distributed circuit within the piriform cortex makes odor discrimination robust. J. Comp. Neurol. 526, 2725–2743.

Suarez, R., Gobius, I., Richards, L.J., 2014. Evolution and development of interhemispheric connections in the vertebrate forebrain. Front. Hum. Neurosci. 8, 497.

Terrigno, M., Bertacchi, M., Pandolfini, L., Baumgart, M., Calvello, M., Cellerino, A., Studer, M., Cremisi, F., 2018. The microRNA miR-21 is a mediator of FGF8 action on cortical COUP-TFI translation. Stem Cell Rep. 11, 756–769.

Tocco, C., Bertacchi, M., Studer, M., 2021. Structural and functional aspects of the neurodevelopmental gene NR2F1: from animal models to human pathology. Front. Mol. Neurosci. 14, 767965.

Tocco, C., Ovsthus, M., Bjaalie, J.G., Leergaard, T.B., Studer, M., 2022. The topography of corticopontine projections is controlled by postmitotic expression of the area-mapping gene Nr2f1. Development 149.

Tole, S., Gutin, G., Bhatnagar, L., Remedios, R., Hebert, J.M., 2006. Development of midline cell types and commissural axon tracts requires Fgfr1 in the cerebrum. Dev. Biol. 289, 141–151.

Tomassy, G.S., De Leonibus, E., Jabaudon, D., Lodato, S., Alfano, C., Mele, A., Macklis, J. D., Studer, M., 2010. Area-specific temporal control of corticospinal motor neuron differentiation by COUP-TFI. Proc. Natl. Acad. Sci. USA 107, 3576–3581.

Wang, F., Zhu, J., Zhu, H., Zhang, Q., Lin, Z., Hu, H., 2011. Bidirectional control of social hierarchy by synaptic efficacy in medial prefrontal cortex. Science 334, 693–697.

Wang, L., Zhang, Z., Chen, J., Manyande, A., Haddad, R., Liu, Q., Xu, F., 2020. Cell-type-specific whole-brain direct inputs to the anterior and posterior piriform cortex. Front. Neural Circuits 14, 4.

Witter, M.P., 2006. Connections of the subiculum of the rat: topography in relation to columnar and laminar organization. Behav. Brain Res. 174, 251–264.

Yang, W., Sun, Q.Q., 2015. Hierarchical organization of long-range circuits in the olfactory cortices. Phys. Rep. 3.

Yen, C., Lin, C.L., Chiang, M.C., 2023. Exploring the Frontiers of neuroimaging: a review of recent advances in understanding brain functioning and disorders. Life (Basel) 13.

Zeidler, S., Pop, A.S., Jaafar, I.A., de Boer, H., Buijsen, R.A.M., de Esch, C.E.F., Nieuwenhuizen-Bakker, I., Hukema, R.K., Willemsen, R., 2018. Paradoxical effect of baclofen on social behavior in the fragile X syndrome mouse model. Brain Behav. 8, e00991.

Zhang, K., Yu, F., Zhu, J., Han, S., Chen, J., Wu, X., Chen, Y., Shen, T., Liao, J., Guo, W., et al., 2020. Imbalance of excitatory/inhibitory neuron differentiation in neurodevelopmental disorders with an NR2F1 point mutation. Cell Rep. 31, 107521.

Zhang, W., Luo, P., Liu, X., Cheng, R., Zhang, S., Qian, X., Liu, F., 2023. Roles of fibroblast growth factors in the axon guidance. Int. J. Mol. Sci. 24.

Zhou, J., Wen, Y., She, L., Sui, Y.N., Liu, L., Richards, L.J., Poo, M.M., 2013. Axon position within the corpus callosum determines contralateral cortical projection. Proc. Natl. Acad. Sci. USA 110, E2714–E2723.